

CONFERENCES AND SYMPOSIA

PACS numbers: 01.10.Fv, **02.70. – c**, **05.10. – a**, **05.50. + q**, 14.60.St, **23.40. – s**, **31.10. + z**, 42.55.Lt, 42.60.Lh, 52.50.Jm

Modern problems in the physical sciences
(Scientific session of the Physical Sciences Division of the Russian Academy of Sciences, 23 November 2011)

DOI: 10.3367/UFNe.0182.201207g.0773

On 23 November 2011, the scientific session of the Physical Sciences Division of the Russian Academy of Sciences (RAS) was held at the conference hall of the Lebedev Physical Institute, RAS.

The following reports were put on the session agenda posted on the website www.gpad.ac.ru of the RAS Physical Sciences Division:

(1) **Ionin A A** (Lebedev Physical Institute, RAS, Moscow) "High-power infrared and ultraviolet lasers and their applications";

(2) **Romanovskii M Yu** (Prokhorov General Physics Institute, RAS, Moscow) "Laser-induced acceleration of the forbidden captures of orbital electrons by nuclei";

(3) **Petrukovich A A** (Space Research Institute, RAS, Moscow) "Earth's magnetosphere as a plasma laboratory";

(4) **Shchur L N** (Landau Institute for Theoretical Physics, RAS, Chernogolovka, Moscow region) "Computational physics and the verification of theoretical predictions".

Articles written on the base of oral reports 1, 2, and 4 are published below.

PACS numbers: 42.55.Lt, 42.60.Lh, 52.50.Jm
DOI: 10.3367/UFNe.0182.201207h.0773

High-power IR- and UV-laser systems and their applications

A A Ionin

1. Introduction. A brief historical outline of studies made at the Laboratory of Gas Lasers at the Lebedev Physical Institute

The term 'high-power' laser is quite vague, especially for pulsed lasers with high peak powers. For cw and repetitively pulsed high-power lasers, the lower range limit can be conditionally accepted to be ~ 1 kW of average output power, while this limit for pulsed lasers can be estimated by the peak power of ~ 1 MW. The maximum average power has been achieved in megawatt lasers [1], while the maximum peak power of about 1 PW has been generated in femtosecond laser pulses [2]. At present, femtosecond pulsed lasers with peak powers of up to ~ 10 PW are being developed, and the possibility of creating exawatt pulsed lasers is being discussed [2]. In this paper, mainly IR and UV lasers developed, investigated, and exploited in studying the interaction of radiation with matter at the Laboratory of Gas Lasers (LGL) at the Lebedev Physical Institute, RAS (FIAN in *Russ. abbr.*) with the participation of the author are considered.

The Laboratory was founded by N G Basov (1922–2001) in the early 1980s for studying the physical principles of exploring high-power industrial and defense-purposes lasers. Researchers at the Laboratory took part in the development of a megawatt class CO_2 laser [1] and 10–30-kW average-power industrial CO_2 and CO lasers. The main avenues of research conducted at the LGL are the development of excimer lasers, atomic-transition lasers, molecular lasers, and the interaction of laser radiation with matter.

Researchers at the LGL have created a variety of large-scale lasers, such as an electron-beam-pumped KrF laser (under the supervision of V D Zvorykin) with an active volume of about 20 l emitting 0.248-μm, 100-J, 100-ns pulses; electron-beam-pumped and electron-beam-controlled atomic transition pulsed lasers (under the supervision of I V Kholin) comprising a 1.73-μm, 80-J Ar/Xe laser, 1.27-μm, 4.5-J He/Ar laser, 2.52-μm, 4-J He/Kr laser, and 0.58-μm, 1.5-J He/Ne laser; and pulsed electron-beam-controlled molecular lasers (under the supervision of the author of this paper) comprising a 10.6-μm, 500-J CO_2 laser, a fundamental-transition 5–6-μm, 800-J CO laser and overtone-transition 3-μm, 50-J CO laser, an N_2O laser ($\lambda = 10.9$ μm, $Q = 100$ J), and a quasi-cw supersonic 100-kW CO laser emitting 1-ms pulses [4]. A group of researchers at the Laboratory headed by B I Vasil'ev have proposed the scheme and developed the design of a two-frequency differential-absorption lidar, in which the reference beam is formed by radiation from a CO_2 laser and the operating-beam radiation can be sequentially tuned over lines in the spectrum of an NH_3 laser [3].

The Laboratory of Gas Lasers at FIAN has actively collaborated and continues to collaborate with foreign institutions in the advancement of laser technologies. In 1992–1996, researchers of the Laboratory were involved, together with colleagues from Great Britain and France, in the Eureka-113 CO-Eurolaser European project [5] on the development of high-power industrial CO lasers. In 1994, researchers at the Institute of Technical Physics (Stuttgart,

A A Ionin Lebedev Physical Institute, Russian Academy of Sciences, Moscow, Russian Federation
E-mail: aion@sci.lebedev.ru

Uspekhi Fizicheskikh Nauk **182** (7) 773 – 792 (2012)
DOI: 10.3367/UFNr.0182.201207g.0773
Translated by V I Kisin, Yu V Morozov, M Sapozhnikov; edited by A Radzig

Uspekhi Fizicheskikh Nauk **182** (7) 773 – 781 (2012)
DOI: 10.3367/UFNr.0182.201207h.0773
Translated by M Sapozhnikov; edited by A Radzig

Germany), in collaboration with research workers from the LGL, put into service a repetitively pulsed CO laser operating at room temperature with an average of about 1-kW output power [6]. In 1995–1998, the Laboratory participated in the Eureka-1390 Ultralas European project (Russia, Austria, Germany, and some others) aimed at the establishment of principles for the construction of a 100-kW industrial CO_2 laser.

In 1995–1996, together with colleagues at the Directorate of Applied Technology, Test and Simulation (DATTS) (White Sands proving ground, USA) and using the equipment brought by them, researchers at the LGL investigated the phase conjugation for radiation from CO_2 and CO lasers created at the LGL [7]. The same lasers were used in 1995–1997 in the team work with DuPont (Wilmington, USA) on the laser modification of the surface of synthetic fabrics by exposing the surface of nylon and Dacron fibers to frequency-selective radiation from a CO laser at a wavelength of ≈ 6 μm to eliminate so-called synthetic gloss [8], and in 1997–1999 for collaborative studies with the Colorado School of Mines (Golden, USA) on the interaction of radiation from high-power IR lasers with oil-bearing rocks [9], within the framework of a project on estimating the possibility of the manufacture of laser drilling rigs.

Later projects on developing, along with the University of New Mexico and the Air Force Research Laboratory (AFRL) (Albuquerque, USA), a supersonic CO laser operating on fundamental and overtone transitions in the CO molecule and studying electric-discharge generators of a singlet-oxygen energy donor for an oxygen–iodine laser and an electric discharge controlled by combined femtosecond and nanosecond UV pulses from a hybrid KrF-laser system, which were supported by partnership projects of the International Science and Technology Center (ISTC) with the European Office of Aerospace Research & Development (EOARD), are discussed in Sections 2–5.

2. Infrared carbon monoxide lasers and their application

Carbon monoxide (CO) lasers [which should be distinguished from carbon dioxide (CO_2) lasers] are of interest both for the creation of high-power mid-IR coherent radiation sources and for studying molecular kinetics, because the population inversion between the vibrational–rotational levels of the CO molecule is produced due to the vibrational–vibrational energy exchange between CO molecules which constitute pronounced anharmonic oscillators. The CO laser can emit at $\sim 10^3$ vibrational–rotational spectral lines in fundamental vibrational bands with a change in the vibrational quantum number by unity in the spectral range from 4.6 to 8.2 μm and at the first overtones in the wavelength range from 2.5 to 4.2 μm. The history of the advent and evolution of CO lasers and the physical principles of their operation (in particular, the reasons for the necessity of cooling the active medium of the laser) are presented in review [10].

The emission region of an overtone CO laser covers 'the transparency window' of the terrestrial atmosphere in the wavelength range from ≈ 3.3 to 4.0 μm, and therefore this laser can be utilized for the transport of high-power radiation in the atmosphere. Because a huge number of the emission lines of the CO laser lie in spectral regions where the absorption lines of many explosives and toxic substances are located, CO lasers, not necessarily with high output powers, can be used for a multicomponent gas analysis of these and other substances.

Research into CO lasers at the LGL has been concentrated during the last decade on the following areas: the creation and exploration, in joint work with colleagues from the USA, a supersonic CO laser, in particular, an overtone laser; the development of a compact CO laser tunable in the 5-μm wavelength range and emitting at overtone transitions in the region from 2.5 to 4.0 μm upon pumping by a high-frequency (radio-frequency or RF) slab discharge; the creation of a CO-laser system generating nanosecond pulses; and the estimation of the possibility of CO laser applications for laser uranium isotope separation.

2.1 Supersonic overtone CO laser

A supersonic overtone CO laser with the active medium cooled during its adiabatic expansion in a supersonic nozzle was developed and investigated within the framework of collaborative ISTC projects Nos 1865 and 2415 based on recommendations formulated at the LGL, where the operation of the supersonic CO laser launched at the AFRL was simulated theoretically and experimentally. These studies have revealed that the overtone CO laser can emit in high-lying vibrational bands, up to the $38 \rightarrow 36$ transition, at more than 400 spectral lines in the selective mode and with an efficiency up to 16% in the multifrequency mode (see, for example, Ref. [11]). The setup at the AFRL was initially constructed based on a high-frequency-discharge-pumped supersonic CO laser with an output power of 330 W (with a single-pass cavity) developed at the Institute of Technical Physics in Stuttgart. The design of the setup was considerably changed in collaborative work with American and German colleagues [12] by retaining its active volume (the active length measured 10 cm, the Mach number in a supersonic flow reached 2.7, the gas temperature and pressure in the stream were ≈ 100 K and 2–9 Torr, respectively, and the output power at fundamental transitions (≈ 5 μm) achieved 2.1 kW with an efficiency of 21% (for a single-pass cavity). For overtone transitions, 50 W of output power were achieved in the case of highly reflecting mirrors. Estimates showed that the output power of an overtone CO laser with the optimal cavity can approach 500 W.

2.2 High-frequency-discharge-pumped compact slab CO laser

Recently, considerable progress has been achieved in the advancement of diffusion-cooled capillary and slab gas lasers (including gas-flow and sealed CO_2 and CO lasers) excited by a capacitive transverse RF discharge. In these lasers, heat is removed from a gas mixture through cooled electrodes to which the exciting high-frequency voltage is applied. The RF discharge offers a number of advantages compared to the simple and often used dc discharge. The CO laser is known to demonstrate the highest output characteristics at cryogenic temperatures of the active gas mixture. This is especially inherent in the overtone CO laser [13]. An important practical problem consists in the development of a compact RF discharge-pumped slab CO laser with the active medium diffusively cooled to low temperatures. Such a laser, combining relative simplicity and compactness inherent in slab RF designs and the high efficiency and a broad emission spectrum typical of electric-discharge CO lasers, can become a unique spectroscopic tool for detecting various explosives, toxics, and other hazardous substances and materials.

Researchers at the LGL have developed compact RF-discharge pumped slab CO lasers with cryogenically cooled electrodes and different active-medium lengths (250 and 400 mm) [14]. Optimal conditions (the gas-mixture composition and pressure, RF discharge parameters) were established for obtaining the best laser output characteristics. The maximum mean power output of the fundamental-transition CO laser (in the spectral range from 5.1 to 5.4 μm) was ≈ 12 W, with the efficiency achieving ≈ 14%. This laser can also operate in the frequency-selective mode. Single-frequency lasing was observed at approximately 100 spectral lines in the wavelength range from 4.9 to 6.5 μm with a mean power output from a few milliwatts to a few dozen milliwatts. Researchers at the LGL have obtained for the first time lasing in an RF-discharge pumped slab cryogenic CO laser at overtone transitions in the CO molecule in the spectral range from 2.5 to 4.0 μm [14].

By optimizing experimental parameters in the free-running multifrequency lasing regime, the author of this paper, together with A Yu Kozlov, L V Seleznev, and D V Sinitsyn (FIAN), has recently achieved a mean power of ≈ 1.8 W in the spectral range from 2.95 to 3.45 μm, with an efficiency up to 1.5%. All the results were produced without the forced replacement of a gas mixture. Under fixed experimental conditions, stable lasing (with output characteristics fluctuating within 10%) was obtained in the time interval exceeding an hour, which demonstrated for the first time the operation of a cryogenic CO laser in the sealed mode. The tuning range of the CO laser overlaps the spectral regions comprising the absorption lines and bands of usual substances (H_2O, CO_2, O_3, N_2O, NO_2, NO, SO_2, NH_3, etc.), organic compounds (methane, acetone, benzene, methanol, ethanol, etc.), and strong contaminants.

A CO laser operating on many spectral lines is an attractive radiation source for spectral analysis of multicomponent gas mixtures and individual substances present in the atmosphere. The overtone CO laser was used in model experiments on measuring the concentration of gases in the two-component mixture ($N_2O + CH_4$) in the region of the overlap of their absorption spectra (Fig. 1). It was demonstrated that the accuracy of recovering the concentration of gases in a multicomponent mixture increased upon increasing the number of laser lines involved in measurements.

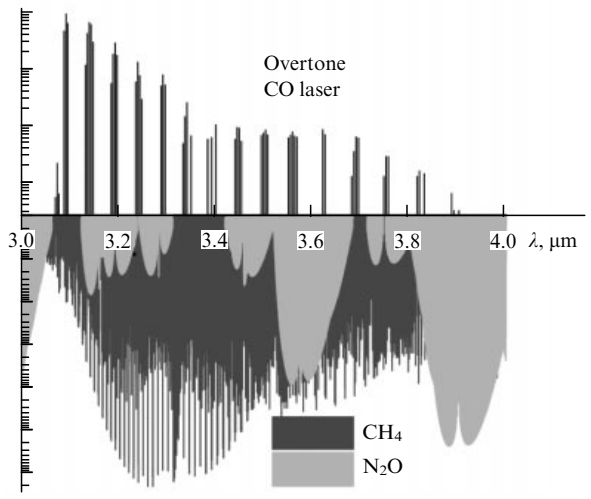

Figure 1. Typical emission spectrum of an overtone CO laser and absorption spectra of methane (CH_4) and nitrous oxide (N_2O).

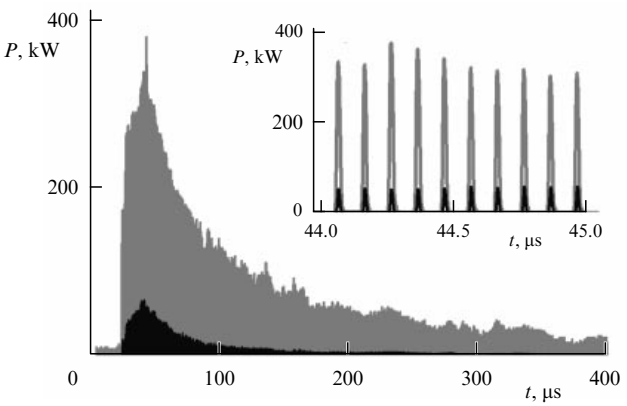

Figure 2. Train of nanosecond pulses at the input (dark color) and output (grey color) of the CO laser amplifier.

2.3 Nanosecond master oscillator–laser amplifier CO laser system

The laser levels of the CO molecule are populated due to a comparatively slow vibrational energy exchange between colliding molecules, and therefore it was assumed until recently that the mode-locked CO laser operating on vibrational–rotational transitions exhibits a low efficiency. However, high-power nanosecond pulses at ~ 5 μm proved to be required for solving the complex scientific and technical problem of stochastic cooling of relativistic ions in colliders. It was demonstrated in paper [15] that our electron–beam-controlled, actively mode-locked, cryogenic CO laser could generate a train of 5–15-ns pulses at a repetition rate of 10 MHz, equal to the repetition rate of ion bunches in the RHIC (Relativistic Heavy Ion Collider) at the Brookhaven National Laboratory (USA). The peak power output of this laser achieved 120 kW in the multifrequency mode (≈ 29 spectral lines), and 70 kW in the frequency-selective mode for lasing at the $9 \rightarrow 8P(11)$ transition line. The output peak power of the CO laser was increased to 380 kW in the multifrequency mode (Fig. 2) and to 130 kW in the frequency-selective mode by employing a specially developed master oscillator–laser amplifier system [16]. The study of the amplification of short laser pulses gave evidence that, due to the high rotation relaxation rate, the gain saturation intensity at a spectral line in the CO laser amplifier was ≈ 14 kW cm^{-2}, which exceeds the gain saturation intensity in a multifrequency cw CO laser by a few orders of magnitude.

2.4 Uranium isotope separation by means of CO lasers

Until recently, the CO laser was considered only as a promising radiation source for exciting photochemical reactions accompanying the separation of uranium isotopes, because several lines of this laser near $\lambda = 5.3$ μm fall into the $3\nu_3$ absorption band of uranium hexafluoride (UF_6) molecules [17] and can isotope-selectively initiate chemical reactions [18]. However, the situation changed dramatically when it was shown that short pulses from a mode-locked CO laser have a high peak power [15, 16] and, therefore, can be converted in nonlinear optical crystals to other spectral ranges. For example, the internal second-harmonic conversion coefficient for the CO-laser radiation in a $ZnGeP_2$ crystal achieved 25% [19, 20], which confirms the possibility of the efficient radiation frequency conversion by summation and subtraction of the CO-laser radiation frequencies. All the more because the CO laser can emit approximately 1000 lines

in the frequency-selective mode in a wide wavelength range from 2.5 to 8.3 μm. Due to such unique properties, CO-laser radiation can be converted to fall to the absorption bands of uranium hexafluoride molecules wherein the isotope shift is present, which is necessary for the laser separation of uranium isotopes, including the ν_3 band with the high absorption cross section near 16 μm [17]. Thus, the CO laser with radiation conversion in nonlinear optical crystals can become the efficient radiation source for uranium isotope separation.

3. Problem of the development of an electric-discharge IR oxygen–iodine laser

Chemical oxygen–iodine lasers (COILs) utilize singlet oxygen molecules $O_2(a^1\Delta_g)$ as energy donors for atomic iodine emitting laser radiation. However, the application of COILs is restricted due to the necessity of using toxic substances for obtaining singlet oxygen molecules in a chemical generator. One of the alternative methods for generating singlet oxygen is its production in an electric discharge. Lasing in the electric-discharge oxygen–iodine laser was first obtained by exciting an oxygen-containing gas mixture and producing singlet oxygen in a radio-frequency discharge, which was followed by mixing singlet oxygen in a laser mixture with iodine and cooling the mixture in a supersonic flow [21]. Singlet oxygen has been produced in an electric-discharge singlet-oxygen generator. Then, the singlet oxygen is transported to a region of mixing with iodine atoms supplied by iodine-containing molecules. Lasing at a wavelength of 1.316 μm appears directly after mixing singlet oxygen with atomic iodine in the laser cavity. The cooling of the gas mixture to cryogenic temperatures provides a positive gain for a considerably smaller singlet-oxygen yield $Y = [O_2(a^1\Delta_g)]/([O_2(X^3\Sigma_g^-)] + [O_2(a^1\Delta_g)])$, approaching $Y_{th} \approx 1\%$ at $T = 100$ K. For comparison, $Y_{th} \approx 15\%$ at $T = 300$ K. (The physics and techniques of producing singlet oxygen in an electric discharge, in particular, in a radio-frequency discharge, are described in detail in review [22].) At present, the maximum power output of the electric-discharge oxygen–iodine laser equals ≈ 500 W [23]. The U.S. Defense Advanced Research Projects Agency (DARPA) supports projects on the creation of a 100-kW oxygen–iodine laser with a lasing efficiency of ≈ 10% [24].

Experimental studies on the energy characteristics of an electric singlet-oxygen generator based on a pulsed e-beam sustained discharge in oxygen-containing gas mixtures showed that the addition of CO or H_2 to a gas mixture of O_2 and Ar considerably improved the stability of the discharge, providing a high specific energy input (the maximum value recalculated to the molecular components of the mixture reached ≈ 6.5 kJ l^{-1} atm^{-1} (≈ 150 kJ mol^{-1}) in the O_2:Ar:CO gas mixtures (1:1:0.1) at a total gas pressure of 30 Torr and an excitation volume of about 18 l [25]). It was predicted theoretically that, by using mixtures with CO, H_2, or D_2 molecular additions in an e-beam sustained discharge, one can expect a yield of singlet oxygen $O_2(a^1\Delta_g)$ reaching approximately 25%, which exceeds the value required for the operation of the oxygen–iodine laser at room temperature [25].

To study the production and relaxation of singlet oxygen molecules in a subsonic gas flow excited by a transverse slab radio-frequency discharge, an original experimental setup was developed within the framework of collaborative ISTC project No. 3835 (Fig. 3). Experimental results and numerical

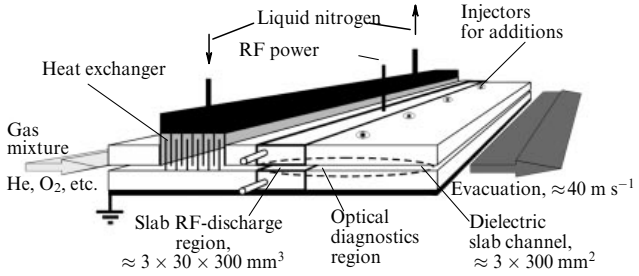

Figure 3. Schematic of an electric-discharge singlet-oxygen generator based on a gas-flow slab setup with transverse radio-frequency excitation and the possibility of the cryogenic cooling of electrodes.

simulations [26] suggest that it is possible to obtain lasing in the oxygen–iodine laser with an electric-discharge singlet-oxygen generator based on a transverse RF discharge upon cooling the excited gas down to ≈ 220 K, which is quite real even without the employment of a supersonic expansion of the gas flow.

4. The hybrid system of UV Ti:Sa–KrF lasers

To study the interaction of femtosecond laser pulses with matter, researchers at the LGL developed a hybrid solid-state–gas laser system [27] consisting of a Ti:Sa start-up laser and electron-beam KrF laser amplifiers built earlier (see the Introduction and Ref. [3]). A specific feature of hybrid systems is that femtosecond pulses generated by a solid-state laser and passed through a prism stretcher with negative dispersion are directly amplified in gaseous active media without recourse to the complicated and expensive optical compressors based on diffraction gratings, followed by their compression through the agency of plane-parallel plates with positive dispersion. The hybrid laser system consists of a solid-state start-up laser complex generating femtosecond pulses, a KrF laser preamplifier, and a final amplifier.

A solid-state start-up facility emitting UV femtosecond pulses was designed and fabricated by Avesta-Project, a Russian company, in collaboration with researchers at FIAN. This facility, consisting of a 744-nm, 30-fs Ti:Sa laser, an optical stretcher, a regenerative amplifier, multi-pass amplifiers, an optical compressor, and a third-harmonic optical converter, emits 0.5-mJ, 60–100-fs pulses at 248 nm with a pulse repetition rate of 10 Hz. The laser beam diameter measures 8 mm. The maximum output radiation energy at the fundamental wavelength reaches 8 mJ. This facility can also generate 2-mJ second-harmonic femtosecond pulses at 372 nm. The electron-beam-pumped KrF laser preamplifier [27] has an active volume of $10 \times 10 \times 100$ cm^3. The final KrF laser amplifier [27] with an active volume of $16 \times 18 \times 100$ cm^3 is pumped by two counterpropagating electron beams generated by two electron guns and directed to a laser chamber through a titanium foil.

This hybrid laser setup was drawn in to study the amplification of ultrashort UV pulses in the two stages of electron-beam-pumped wide-aperture KrF amplifiers [28]. The total output energy of the preamplifier reached 23 mJ and the beam cross section area (38.5 cm^2) was about 60% of the preamplifier aperture. The ultrashort pulse energy at the final amplifier output amounted to 0.62 J under saturation conditions in a laser beam 92.5 cm^2 in cross-section area,

comprising 43% of the amplifier aperture. The input pulse incident on the preamplifier was ≈ 100 fs in duration, i.e. a stretcher was not used after beam exit from the start-up facility. The pulse duration at the final amplifier output, measured with an image-converter camera, did not exceed 1 ps and was no shorter than ≈ 330 fs (measurement of the coherence length). Thus, the pulse peak power reached ≈ 1 TW. The angular divergence of radiation was 20 μrad. Estimates show that, for an aperture filling factor equal to 1.0, the energy of the amplified pulse will reach ~ 1.5 J. The employment of a stretcher for the pulse of ≈ 60 fs in duration at the output of the start-up facility will provide laser pulses of $\sim 20-30$ TW in peak power at the system's output.

5. Interaction of femtosecond infrared and ultraviolet radiation pulses with matter

5.1 Filamentation of femtosecond pulses and ionization of gases by these pulses

The problem of amplification of ultrashort UV laser pulses in electron-beam KrF amplifiers proved to be closely related to processes of the nonlinear propagation of high-power UV laser pulses in the atmosphere, gases, and transmissive (transparent) optical elements. Experiments confirmed the existence of nonlinear absorption of comparatively low-intensity UV radiation, while investigations of the multi-photon ionization of pure gases (argon and nitrogen) [29] revealed that an increase in UV laser radiation intensity above 10^{12} W cm^{-2} leads to an increase in the number of photons participating in the nonlinear process from 3 to 4 quanta. It seems that this change is caused by a change in the ionization process. Thus, for low intensities (from $\approx 3 \times 10^{10}$ to 2×10^{11} W cm^{-2}), high-lying electron states are excited by three photons, and then one-photon ionization follows. As the radiation intensity is increased, the high-lying electron levels shift due to the dynamic Stark effect and 'exit' the three-photon resonance. As a result, nonresonance four-photon ionization is observed.

By using the method of time-resolved optical microscopy, researchers at the LGL have demonstrated the existence of a single or many short (down to 100 μm) and narrow (down to 5 μm in diameter) minifilaments of strongly focused ultrashort IR laser pulses in air [30]. The length of luminous plasma channels considerably exceeded the corresponding length of the focal waist. The plasma density estimated by various methods proved to be rather high (up to 10^{18} cm^{-3}). The existence of such minifilaments was previously subjected to question by leading researchers in this field, because earlier experimental examinations with weakly focused ultrashort pulses gave considerably greater lengths and diameters of gas (air) filaments (up to a few dozen meters and hundreds of micrometers, respectively). Numerical simulations for such conditions were performed at the Zuev Institute of Atmospheric Optics, SB RAS [31]. The results of numerical calculations confirmed the existence of mini-filaments produced by ultrashort pulses and also gave a systematic description of the fundamental mechanisms of producing minifilaments by strongly focused ultrashort pulses and their basic dimensional and energy parameters (the maximum intensity and plasma density in a filament).

Researchers at the LGL have performed a number of studies on the possibility of applications of minifilaments. Thus, experiments were performed on the generation of a third harmonic in air minifilaments. In particular, it was shown that the maximum conversion efficiency of strongly focused IR ultrashort pulses to third-harmonic UV ultrashort pulses could reach 0.16% [32]. The very strong focusing (numerical apertures of focusing optics down to 0.65) of laser pulses was used for the advancement of the innovation technology for microscale volume labeling of natural diamonds [by recording graphite microchannels; this work was performed in collaboration with the Kristall Industrial Association (Smolensk)] [33] and import-replacing medical technology for volume microscopic perforation of eye tissues for microsurgical vision correction by cornea shaping and nearly noninvasive removal of malignant tumors on the sclera (this work was performed in collaboration with the Central Clinical Hospital, RAS) [34]. Notice that practical technologies for microscopic labeling and eye microsurgery have been preceded by the fundamental studies into the physical mechanisms of producing microscopic damage in materials, and the peculiarities and parameters of microfilamentation in transparent media.

5.2 Nanophotonics of the nanostructured surfaces and bulk photonic crystals

Although the laser-induced fabrication of one-dimensional periodic surface nanostructures (PSNSs) under the action of ultrashort (femtosecond) laser pulses have been studied already for more than a decade, the PSNS fabrication mechanisms, in particular, dynamic changes in the optical properties of the optically excited surface of materials, the distribution of the electromagnetic field energy due to the interference of ultrashort pulses with a surface electromagnetic wave (SEW) excited by these pulses, mass transfer mechanisms (material removal due to ablation), the optics of a photoexcited nanostructured surface, and the appearance of subwavelength ($\Lambda \ll \lambda$, where λ and Λ are the wavelengths of the incident radiation and produced periodic structure, respectively) PSNSs have been investigated inadequately to date. Because of this, we examined the following main stages of the PSNS fabrication by ultrashort pulses [35–43]:

(1) the photoexcitation of a surface and interference of ultrashort pulses with SEWs subjected to IR and, for the first time, UV ultrashort pulses [35–37, 42];

(2) the appearance of the primary, as a rule, anharmonic, near-wavelength ($\Lambda \approx \lambda$) periodic nanorelief [35, 37];

(3) recording PSNSs (including subwavelength nanogratings) due to the diffraction of ultrashort pulses by the primary anharmonic nanorelief [35, 37, 38, 40–43];

(4) the fabrication of PSNSs during the interaction of multiple subsequent ultrashort pulses with a developed nanorelief, up to its degradation and formation of a microrelief [39–42].

A simple and informative method was proposed for studying the dynamic optical constants of matter on the ultrashort-pulse scale by measuring pulse self-reflection [35–37]. The higher harmonics of a nanorelief (up to the 7th harmonic) were observed for the first time [35, 37], and the fabrication of such subwavelength PSNSs was explained not by the unlikely generation of higher optical surface harmonics, but via the diffraction of ultrashort pulses by the primary anharmonic nanorelief (the superposition of nanorelief harmonics) which appears, as a rule, in a slightly above-threshold regime of nanostructuring, with the excitation of a set of SEWs with the corresponding wave-number spectrum [35, 37].

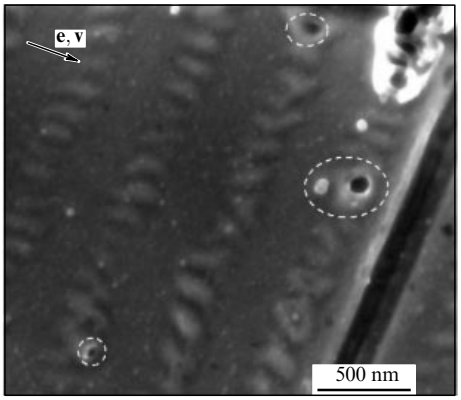

Figure 4. Nanostructures fabricated on an aluminium surface at the irradiation power density $F = 0.5$ J cm^{-2} and $N = 500$. The image was obtained with a scanning electron microscope with magnification 120,000. The arrow shows the direction of the polarization vector **e** of the laser field and the velocity vector **v** of a target. The dashed contours single out nanospikes with craters instead of a top and material removal traces.

In addition, the study of PSNS fabrication by ultrashort pulses with energy densities lying slightly below the threshold revealed not the regular sequences of nanorelief grooves but two-dimensional arrays of nanospikes (Fig. 4), the latter periodically appearing in the lines of the ultrashort-pulse–SEW interference maxima due to the cavitation instability of a surface melt [43] (the possibility of the formation of a nonperiodic nanorelief had been predicted earlier in calculations by the molecular dynamics method). The microscopic cavitation dynamics mechanism preceding the formation of nanospikes due to a partial 'frozen' split-off of a part of a surface melt film, as well as other microscopic mechanisms of the split-off and fragmentation ablations of solids under the action of ultrashort pulses, was first investigated by our team with the method of time-resolved optical microscopy in paper [44].

The results of this study demonstrated for the first time the possibility of monitoring the motion of the melting front in a material by observing acoustic reverberations in a surface melt film with the acoustic impedance different from the impedance of the solid material, and also the motion of the cavitation region from the surface to the melt volume caused by the surface cooling during its adiabatic expansion, followed by the split-off and extrusion of a cooled surface layer from the target surface on the subnanosecond time scale, probably mainly due to the vapor pressure in the cavitation region under the surface (nanofoam) rather than stress (rarefaction) waves circulating in the melt. Upon irradiation by ultrashort pulses with higher energy densities, we observed the irreversible fragmentation removal of a higher-temperature surface melt layer due to its cavitation.

The fragmentation mechanism of surface ablation of solid materials caused by ultrashort laser pulses and the higher-energy mechanism of their ablation via direct ionization were also examined by the method of contactless broadband ultrasonic diagnostics adapted for detecting superpower shock waves generated during ablation produced by above-mentioned pulses. It is known that during the propagation of superpower shock waves in materials, these materials experience plastic deformation (elastoplastic transition) and polymorphic transformations caused by the shock-wave loading. As a result, the profile of a propagating shock wave gradually changes, even in rather thin (submicron and micron thick) targets, which proves to be especially considerable in the case of generation of superpower shock waves during the ablation of targets caused by high-intensity ultrashort pulses with peak intensities up to 0.1–1 PW cm^{-2}. Because of this, we proposed a new approach to the study of superpower shock waves generated during the ablation of materials by high-intensity ultrashort laser pulses, which is based on the observation of the shock-wave evolution in a bordering medium with high shock-wave and optical strength, for example, in air [45].

We implemented the experimental scheme of recording superpower shock waves by the method of contactless broadband ultrasonic diagnostics by observing the propagation of shock waves *in air* from a surface being ablated to a broadband piezoelectric detector [45–47]. This scheme is devoid of the dimensional target-thickness effect and also allows one to investigate *in situ* a variety of materials with different surface reliefs with micrometer spatial resolution. We performed table-top investigations of superpower sub- and multimegabarn shock waves excited on an aluminium surface ablated in air under the action of high-intensity ($\leqslant 1$ PW cm^{-2}) linearly polarized ultrashort laser pulses [45]. The estimates of the initial pressure and velocity of a shock wave (the ablation torch) are in good agreement with data in the literature obtained by different methods for shock waves propagating *inside* a target being ablated (Fig. 5).

Finally, in the last years we have studied the production of sols of chemically 'pure' nanoparticles through the ablation of solid materials such as iron, gold, nickel, silicon, and a superconducting YbCo ceramic irradiated by ultrashort pulses in different liquids. Nanoparticle sols obtained in these experiments found application, in particular, to fabricate nanocomposites based on a three-dimensional photonic crystal dielectric matrix (artificial opal) by filling air nanovoids inside it with quantum dots-nanoparticles and then drying the solvent. The optical spectroscopy of the stop (forbidden) band of opal demonstrates, due to the high chemical purity of the nanoparticles, correct signs and high predictable amplitudes of the 'blue' (for metal nanoparticles) and 'red' (for dielectric nanoparticles) shifts of the band spectrum of the nanocomposite [48].

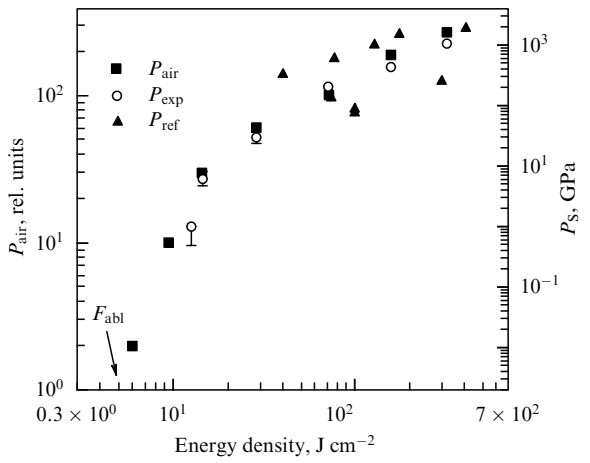

Figure 5. Experimental dependences of the pressure-wave amplitude P_{air} (left ordinate, dark squares) and the initial pressure P_S in the laser torch (right ordinate) on the irradiation energy density F: dots mark our experimental data P_{exp}, and triangles are data P_{ref} from the literature. The arrow shows the material ablation threshold F_{abl}.

5.3 Initiation of electric discharges by combined femtosecond and nanosecond UV laser pulses

Plasma channels produced by laser radiation in the atmospheric air or some other gases are of considerable interest for many fundamental problems and technological applications. Among them are the lightning initiation and active lightning protection, the directional transfer of microwave radiation to reduce its natural divergence, and laser acceleration of electrons. Unlike earlier experiments with submicrosecond CO_2 laser pulses [49], in which absorption in dense plasma produced during avalanche ionization restricted the channel length and continuity, new approaches with the aid of long UV pulses [50] or ultrashort femtosecond pulses [51] allow one to produce extended weakly ionized tracks in gases due to multiphoton ionization and (or) laser beam filamentation. Because primary electrons rapidly recombine with positive ions and attach to oxygen molecules for $\sim 10-50$ ns, it is reasonable to utilize additional visible or UV radiation to maintain the electron density at the desired level for a rather long time. Therefore, the combination of a train of ultrashort high-intense UV laser pulses with long UV pulses looks quite attractive for the production and subsequent maintenance of a plasma channel.

Within the framework of collaborative ISTC project No. 4073, the author and V D Zvorykin, A O Levchenko, S I Kudryashov, L V Seleznev, D V Sinitsyn, and N N Ustinovskii at the LGL developed a new optical scheme for a multistage hybrid Ti:Sa–KrF laser facility emitting trains of ultrashort pulses with a high peak power of 0.2–0.3 TW in combination with 100-ns high-energy pulses [52]. Single ultrashort pulses or a train of these pulses with a period of 5 ns were injected into an unstable confocal cavity of a main wide-aperture KrF-laser amplifier through a semitransparent meniscus, which were amplified in the course of multiple round trips in the cavity and overlapped with a free-running pulse (Fig. 6). The injected 0.5-mJ, 60-fs ultrashort laser pulses at 248.4 nm were generated by a Ti:Sa start-up facility and their energy was increased to ≈ 20 mJ in the KrF-laser preamplifier. The injected ultrashort pulses were amplified during multiple round trips in the cavity against the free-running generation background [their amplitude in Fig. 6 is 1000 times smaller than in reality because of the limited time resolution of a vacuum photodiode (≈ 1 ns) integrating signals of ultrashort pulses ≈ 1 ps in duration]. The energy of combined radiation pulses amounted to $\approx 10-30$ J. We measured the conductivity of plasma channels produced in the atmospheric air by combined UV pulses focused with a spherical mirror with a focal distance of ≈ 8.0 m. We detected a photocurrent signal caused by the electron component of photoionization plasma produced in the transfer region between two circular electrodes separated by a distance of 20 cm, the applied voltage being $U = 5-22$ kV.

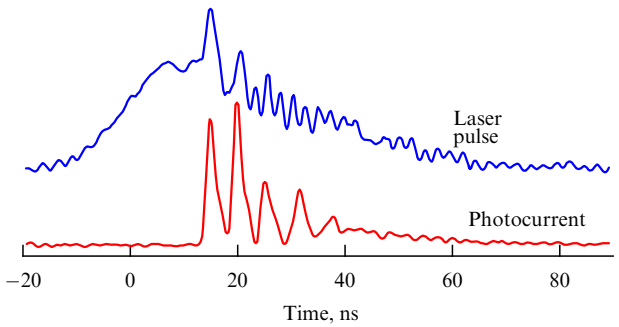

Figure 6. Oscillograms of a combined laser pulse (upper curve) and photocurrent (lower curve) during the injection of a train of ultrashort pulses into the laser cavity [52].

Typical oscillograms of a laser pulse detected with a photodiode (upper curve) and of an electron photocurrent (lower curve) in Fig. 6 show that the current amplitude, which is close to zero at the front of a free-running pulse, drastically increases with the appearance of an ultrashort pulse. The measurement of the electron photocurrent in the case of a 100-ns smooth pulse in the free-running mode (without the injection of ultrashort pulses) gave a photocurrent two orders of magnitude smaller than that in the case of a modulated laser pulse. This is explained by the nonlinear dependence of air photoionization on the laser radiation intensity. When the geometrical focus of the mirror was displaced within ≈ 1.0 m with respect to the interelectrode gap, the photocurrent changed insignificantly, which obviously indicates the filamentation of the ultrashort-pulse laser beam and allows one to estimate the nonlinear propagation length.

Preliminary experiments on the initiation of a breakdown in a discharge gap with a small length [53] showed that a free-running pulse produces electric breakdown in a gap 4.0 cm in length at the applied voltage of 50 kV, with the discharge pulse developing with a ≈ 5-μs delay with respect to the laser pulse, and its propagation direction being not determined by the laser beam. For the same applied voltage, a combined pulse with the same energy provides propagation of the discharge along the beam for a distance of 7 cm, with a delay at least two orders of magnitude smaller. The formation of an extended conducting channel with a comparatively high conductivity maintained by combined UV laser pulses for a few dozen nanoseconds suggests that it is possible to efficiently control a high-voltage breakdown in long air gaps.

6. Conclusion

High-power CO lasers developed in Russian institutions can be utilized for solving many practical problems, including laser uranium-isotope separation. To build a high-power electric-discharge oxygen–iodine laser in Russia, it is necessary to organize the corresponding research and development work. The first experiments with a hybrid terawatt femtosecond UV laser system built in Russia have shown that this system is promising for controling extended electric discharges. During the development of this laser system, we began to study the possibility of applications of femtosecond radiation in medicine and industry, and of changing the surface and bulk properties of solid materials.

References

1. Zarubin P V *Lazernoe Oruzhie — Mif ili Real'nost'? Moshchnye Lazery v SSSR i v Mire* (The Laser Weapon: A Myth or Reality? High-Power Lasers in the USSR and in the World) (Vladimir: OOO "Tranzit-Iks", 2009)
2. Korzhimanov A V et al. *Usp. Fiz. Nauk* **181** 9 (2011) [*Phys. Usp.* **54** 9 (2011)]
3. Ionin A et al. *AIP Conf. Proc.* **664** 697 (2003)
4. Ionin A A et al. *Proc. SPIE* **1397** 453 (1991)
5. Spalding I J et al. *Proc. SPIE* **2713** 103 (1996)
6. Walter S et al. *Kvantovaya Elektron.* **22** 833 (1995) [*Quantum Electron.* **25** 851 (1995)]

7. Beairsto C et al. *Kvantovaya Elektron.* **24** 631 (1997) [*Quantum Electron.* **27** 614 (1997)]
8. Ionin A A, Kleine K R F, Kobsa H *Proc. SPIE* **3092** 422 (1997)
9. Graves R M et al. *Proc. SPIE* **3885** 159 (2000)
10. Ionin A A, in *Gas Lasers* (Eds M Endo, R F Walter) (Boca Raton, Fl.: CRC Press/Taylor and Francis, 2007) p. 201
11. Basov N G et al. *IEEE J. Quantum Electron.* **36** 810 (2000)
12. Bohn W et al. *Kvantovaya Elektron.* **35** 1126 (2005) [*Quantum Electron.* **35** 1126 (2005)]
13. Ionin A A et al. *Laser Phys.* **20** 144 (2010)
14. Ionin A A et al. *IEEE J. Quantum Electron.* **45** 215 (2009)
15. Ionin A A et al. *Opt. Commun.* **282** 294 (2009)
16. Antonyuk E A et al., in *Lazery. Izmereniya. Informatsiya — 2011. Tezisy Dokladov 21-i Mezhdunarod. Konf., St. Petersburg, 7–9 Iyunya 2011 g.* (Proc. of the 21st Intern. Conf. on Lasers, Measurements, and Information, 7–9 June 2011. Abstracts of Papers) Vol. 3 (Ed. V E Privalov) (St. Petersburg: Izd. Politekhnicheskogo Univ., 2011) p. 8
17. Baranov V Yu et al., in *Izotopy: Svoistva, Poluchenie, Primenenie* (Isotopes: Their Properties, Production, and Application) Vol. 1 (Ed. V Yu Baranov) (Moscow: Fizmatlit, 2005) p. 474
18. Eerkens J W, in *Selected Papers on Laser Isotope Separation — Science and Technology* (Ed. J W Eerkens) (Bellingham, Wash.: SPIE Opt. Eng. Press, 1995) p. 531
19. Ionin A A et al. *Laser Phys. Lett.* **8** 723 (2011)
20. Andreev Yu M et al. *Opt. Zh.* **78** (2) 26 (2011) [*J. Opt. Technol.* **78** 102 (2011)]
21. Carroll D L et al. *Appl. Phys. Lett.* **86** 111104 (2005)
22. Ionin A A et al. *J. Phys. D Appl. Phys.* **40** R25 (2007)
23. Carroll D L et al. *Proc. SPIE* **8238** 823803 (2012)
24. Hecht J *Laser Focus World* (9) 41 (2011)
25. Ionin A A et al. *J. Phys. D Appl. Phys.* **36** 982 (2003)
26. Ionin À À et al. *Proc. SPIE* **7581** 758103 (2010)
27. Zvorykin V D et al. *Laser Part. Beams* **25** 435 (2007)
28. Zvorykin V D et al. *J. Phys. Conf. Ser.* **244** 032014 (2010)
29. Ionin A A et al. *Opt. Commun.* **282** 45 (2009)
30. Golosov E V et al. *Pis'ma Zh. Eksp. Teor. Fiz.* **90** 116 (2009) [*JETP Lett.* **90** 107 (2009)]
31. Geints Yu É et al. *Zh. Eksp. Teor. Fiz.* **138** 822 (2010) [*JETP* **111** 724 (2010)]
32. Ionin A A et al. *Laser Phys.* **21** 500 (2011)
33. Ionin A A et al. *Laser Phys.* **20** 1778 (2010)
34. Alekhin A A et al. *Laser Phys. Lett.* **7** 463 (2010)
35. Golosov E V et al. *Zh. Eksp. Teor. Fiz.* **140** 21 (2011) [*JETP* **113** 14 (2011)]
36. Golosov E V et al. *Ross. Nanotekhnol.* **6** (3–4) 82 (2011) [*Nanotechnol. Russia* **6** 237 (2011)]
37. Golosov E V et al. *Phys. Rev. B* **83** 115426 (2011)
38. Golosov E V et al. *Pis'ma Zh. Eksp. Teor. Fiz.* **90** 116 (2009) [*JETP Lett.* **90** 107 (2009)]
39. Golosov E V et al. *Fiz. Khim. Obr. Mater.* (2) 10 (2010)
40. Golosov E V et al. *Appl. Phys. A* **104** 701 (2011)
41. Ionin A A et al. *Kvantovaya Elektron.* **41** 829 (2011) [*Quantum Electron.* **41** 829 (2011)]
42. Korol'kov V P et al. *Kvantovaya Elektron.* **41** 387 (2011) [*Quantum Electron.* **41** 387 (2011)]
43. Ionin A A et al. *Pis'ma Zh. Eksp. Teor. Fiz.* **94** 289 (2011) [*JETP Lett.* **94** 266 (2011)]
44. Ionin A A et al. *Pis'ma Zh. Eksp. Teor. Fiz.* **94** 816 (2011) [*JETP Lett.* **94** 753 (2011)]
45. Ionin A A et al. *Pis'ma Zh. Eksp. Teor. Fiz.* **94** 35 (2011) [*JETP Lett.* **94** 34 (2011)]
46. Ionin A A, Kudryashov S I, Seleznev L V *Phys. Rev. E* **82** 016404 (2010)
47. Ionin A A, Kudryashov S I, Seleznev L V *Kratk. Soobshch. Fiz. FIAN* **38** (6) 13 (2011) [*Bull. Lebedev Phys. Inst.* **38** 161 (2011)]
48. Gorelik V S et al. *Kratk. Soobshch. Fiz. FIAN* **38** (11) 20 (2011) [*Bull. Lebedev Phys. Inst.* **38** 328 (2011)]
49. Koopman D V, Wilkenson T D *J. Appl. Phys.* **42** 1883 (1971)
50. Zhao X M et al. *IEEE J. Quantum Electron.* **31** 599 (1995)
51. Tzortzakis S et al. *Phys. Rev. E* **60** R3505 (1999)
52. Ionin A A et al. *Appl. Phys. Lett.* **100** 104105 (2012)
53. Ionin A A et al., in *High-Power Laser Ablation Conf. HPLA 2012, 28 April–30 May 2012, Santa Fe, NM, USA, 2012*, HPLA Online Book of Procs.

PACS numbers: 14.60.St, **23.40.–s**, **31.10.+z**
DOI: 10.3367/UFNe.0182.201207i.0781

Laser radiation enhancement of forbidden orbital electron captures and of neutrinoless double electron captures by nuclei

M Yu Romanovskii

1. Introduction

The acceleration of the beta decay of particles (a process inverse to electron capture) under the action of an external electromagnetic field has been studied for more than four decades since the pioneering studies [1, 2]. The acceleration of nuclear beta decay was explained by the transformation of the wave function (WF) of a free emitted electron in a (high) electromagnetic field [3–7].[1] In this case, the intensity of an external electric field required for the several-fold acceleration of the process rate was estimated as $E_{\rm crit} = m_{\rm e}^2 c^3/e\hbar \sim 1.3 \times 10^{16}$ V cm^{-1} (where $m_{\rm e}$ is the electron mass, e is the elementary charge, c is the speed of light in vacuum, and $\hbar$ is the Planck constant).

The acceleration of the capture of orbital electrons (a process inverse to beta decay) has not yet drawn significant attention, partly because this effect has been known for a long time (e.g., the rate of the ^{7}Be $\rightarrow$ ^{7}Li process depends on the chemical bond involving a beryllium atom (see Ref. [8]). Furthermore, the theoretically and experimentally studied range of actions on the wave functions of orbital electrons was very wide. It covered the effects of the same chemical bonds and high pressure [9], the thermal effects (including superconductivity), the action of internal electric and magnetic fields of the medium, and plasma effects (see review [10]). K-electron capture was primarily considered, where the possible degree of rate acceleration did not exceed 10^{-2}. The known work (see, e.g., Refs [11–14]) on nuclear excitation accompanying electron transitions in the respective atoms was along the same lines.

The capture of electrons from atomic shells higher than the K-shell is also well known [15–17], including the capture of electrons with a nonzero orbital quantum number l [18, 19]. Just the latter process can be accelerated by an external

[1] Numerous incompletely accurate works predicting the acceleration of beta decay by comparatively moderate external fields are not mentioned here.

M Yu Romanovskii Prokhorov General Physics Institute, Russian Academy of Sciences, Moscow, Russian Federation
E-mail: slon@kapella.gpi.ru

Uspekhi Fizicheskikh Nauk **182** (7) 781–786 (2012)
DOI: 10.3367/UFNr.0182.201207i.0781
Translated by Yu V Morozov; edited by A Radzig

electric field. In the case of a forbidden electron capture, a bound electron–free neutrino pair should compensate for the change in the total angular momentum of the nucleus, i.e., it should be either altered due to the captured orbital electron or 'carried away' by the neutrino. The probability of the transfer of the orbital angular momentum of the electron to the nucleus or carrying away this momentum by the neutrino is determined by two factors. One is the relationship among the nuclear radius, the characteristic radius of the electron wave function, and the de Broglie wavelength of the neutrino. The probability that the orbital angular momentum is carried away by the free neutrino is determined by the ratio of the nuclear radius r_n to the de Broglie wavelength of the neutrino raised to the power of $2l$ (l is the carried away orbital angular momentum). At the same time, the probability of the orbital angular momentum transfer from the orbital electron to the nucleus is determined by the ratio of the nuclear radius to the characteristic radius of the wave function of the orbital electron to the same power $2l$. The second factor is that the orbital electron already carries the angular momentum ready to be transferred to the nucleus, whereas the escaping neutrino has to acquire it during the decay. Then, it follows from the uncertainty relation that this process is rather fast, given the high energies E_ν of the emitted neutrino. Taken together, the above two factors account for the described deceleration of the forbidden capture of orbital electrons. Thus, for $E_\nu < 1$ MeV, the forbidden capture largely involves the corresponding electrons in the p-, d-,... states, i.e., electrons from L_{III}, M_V, N_{VII}, and more deeper-lying shells. A characteristic example is the electron capture by the nucleus of ^{205}Pb: the ratio of K- and L-capture rates is estimated at 10^{-4} [18].

The theory of orbital electron capture by nuclei (see the consistent exposition in monograph [20]) states that probabilities of allowed and unique first-, second-forbidden, etc. captures are proportional to the matrix element squared of the corresponding transition between parent and daughter nuclei, the wave function squared of the electron being captured at the nucleus, the energy of the neutrino raised to the power of 2 for allowed captures, to the power of 4 for the first-forbidden capture, to the power of 6 for the second-forbidden capture, etc., and to the Fermi constant squared of weak interactions. In what follows we will be interested first and foremost in unique first- and second-forbidden transitions expressed through a single nuclear matrix element.[2] Such electron captures are known fairly well. Suffice it to point to the mentioned first-forbidden process in ^{205}Pb. Other quite interesting examples are considered below.

2. The action of an external electric field on electron capture

Among the above terms entering the probability of the electron capture process, only the wave function of the nucleus-bound electron can be affected by an external electric field. Indeed, such a field polarizes the atom, with wave functions of all electrons becoming 'displaced' with respect to the nucleus. Clearly, for electrons in the s-state, this leads only to a decrease in the wave function amplitude at the nucleus where the WFs of such electrons have a maximum. At the same time, there is a point in the nucleus at which wave functions of electrons in the p-, d-,... states vanish. It occurs both in the Dirac description of the single-electron wave functions in an atom and in the description guided by the simple Slater approximation [21, 22]. A polarization shift can only increase densities of electron states of these WF; it is this increase in electron density with a needed orbital momentum at the nucleus that makes possible the acceleration of electron capture rate.

At present, the theory of beta processes [20] is adopting the description of the single-electron state by the Dirac relativistic equation (see, for instance, books [23, 24]) with the self-consistent Hartree–Fock potential. Earlier researchers (up to the 1960s inclusive) made use of electron wave functions in the above-mentioned Slater approximation [25], its main inaccuracy laying just with the failure to take into account relativistic effects. However, it is quite sufficient for our purpose to demonstrate the possibility of acceleration of electron capture by a laser field.

The wave functions in the Slater approximation are written for the purely Coulomb electron–nucleus interaction in the Schrödinger equation. However, this hyperfine interaction causes a certain constant addition to the electron WF to appear at the nucleus. It can be easily shown that at $l = 1$ and 2, i.e., for the first- and second-forbidden electron captures, this addition does not affect the laser radiation-induced acceleration of the above electron captures, while the hyperfine interaction weakens the effect of acceleration starting from the third-forbidden capture.

The correct calculation of the magnitude of electron capture effect from the p-, d-,... states has to include computation of the WFs of these electrons near the nucleus, taking account of the influence of the quasistationary electric field. The perturbation theory may be applied here because the external laser field under such conditions is assumed to be low for $I < Z_{\rm eff}^6 I_0 \sim (10^8 - 10^{10}) I_0$, i.e., in the nonhyperrelativistic case; here, $Z_{\rm eff}$ is the effective shielded charge, $I_0 = cE_{\rm at}^2/8\pi$, $E_{\rm at} = e/r_{\rm B}^2$, and $r_{\rm B}$ is the Bohr radius.

3. Wave functions of electrons at the nucleus in an external electric field

Let us apply the Heisenberg–Schrödinger perturbation theory to elucidate how an external electric field affects the single-particle hydrogen-like Slater wave functions of electrons. Only WF at the nucleus will be needed for the purpose, i.e., at r on the order of several r_n. We shall write out the Schrödinger equation with the effective Coulomb charge and external electric field:

$$\Delta\psi + \frac{2m_e}{\hbar^2}\left(E + \frac{Z_{\rm eff}\, e^2}{r} - eAr\right)\psi = 0\,. \qquad (1)$$

Here, ψ and E are the wave function and the energy of the corresponding electron state, respectively. As usual for problems with an external electric field, we shall move in Eqn (1) to the parabolic coordinates ξ, η, φ (see the best description in Ref. [26]). In these coordinates, the variables are separated, the normalized WF depending on parabolic quantum numbers n_1, n_2, and magnetic number m is expressed in the form

$$\psi_{n_1 n_2 m} = \sqrt{2}\,\varepsilon^{2/3} f_{n_1 m}(\varepsilon\xi) f_{n_2 m}(\varepsilon\eta)\,\frac{\exp(im\varphi)}{\sqrt{2\pi}}\,. \qquad (2)$$

Here, ε, unlike the same quantity in Ref. [20], has the sense of a dimensional constant (inverse effective Bohr radius $r_{\rm B}$): $\varepsilon = Z_{\rm eff}/nr_{\rm B}$, $n = n_1 + n_2 + |m| + 1$ is the principal quantum

[2] For simplicity, we shall consider the action of the electric field on electron capture without regard for exchange and overlap effects. Their influence is pronounced but not decisive [20].

number, functions $f_{n_1 m}$ and $f_{n_2 m}$ satisfy equations

$$\frac{\mathrm{d}}{\mathrm{d}\xi}\left(\xi\,\frac{\mathrm{d}}{\mathrm{d}\xi}\right) f_{n_1 m} + \left(\frac{m_\mathrm{e} E}{2\hbar^2}\,\xi - \frac{m_\mathrm{e} e A}{4\hbar^2}\,\xi^2 - \frac{m^2}{4\xi}\right) f_{n_1 m} = -\beta_1 f_{n_1 m}\,,$$

$$\frac{\mathrm{d}}{\mathrm{d}\eta}\left(\eta\,\frac{\mathrm{d}}{\mathrm{d}\eta}\right) f_{n_2 m} + \left(\frac{m_\mathrm{e} E}{2\hbar^2}\,\eta - \frac{m_\mathrm{e} e A}{4\hbar^2}\,\eta^2 - \frac{m^2}{4\eta}\right) f_{n_2 m} = -\beta_2 f_{n_2 m}\,, \tag{3}$$

$$\beta_1 + \beta_2 = \frac{Z_\mathrm{eff} e^2 m_\mathrm{e}}{2\hbar^2}\,, \qquad \beta_1 = \left(n_1 + \frac{|m|+1}{2}\right)\frac{Z_\mathrm{eff} e^2 m_\mathrm{e}}{2\hbar^2}\,,$$

$$\beta_2 = \left(n_2 + \frac{|m|+1}{2}\right)\frac{Z_\mathrm{eff} e^2 m_\mathrm{e}}{2\hbar^2}\,.$$

As mentioned above, the term with the electric field in Eqn (3) can be regarded as a small perturbation up to the amplitudes as high as the laser field amplitudes: $A < Z_\mathrm{eff}^3 E_\mathrm{at}$, i.e., for all the existing laser systems. Then, the first-order correction to the wave function $f_{n_i m}^{(1)}(x)$ is written as [27]

$$f_{n_i m}^{(1)}(x) = \frac{A}{4Ze\varepsilon^2}\sum_{n_i \neq n_j}\frac{\langle x\rangle_{n_i n_j}^2}{n_i - n_j}\,f_{n_j m}^{(0)}(x)\,, \tag{4}$$

where $f_{n_i m}^{(0)}(x)$ is the solution of equations (3) with $A = 0$, and the matrix element $\langle x\rangle_{n_i n_j}^2$ is the mean of the square of ξ or η over the corresponding unperturbed wave function $f_{n_i m}^{(0)}(x)$ (see Ref. [26] for the values of these matrix elements). The second-order correction $f_{n_i m}^{(2)}(x)$ has a similar form [27]:

$$f_{n_i m}^{(2)}(x) = \frac{A^2}{16Z^2 e^2 \varepsilon^4}\left[\sum_{n_i \neq n_k}\sum_{n_i \neq n_l}\frac{\langle x\rangle_{n_i n_l}^2}{n_k - n_i}\,\frac{\langle x\rangle_{n_l n_k}^2}{n_l - n_i}\,f_{n_k m}^{(0)}(x) - \sum_{n_i \neq n_s}\frac{\langle x\rangle_{n_i n_i}^2\langle x\rangle_{n_i n_s}^2}{(n_s - n_i)^2}\,f_{n_s m}^{(0)}(x) - \frac{1}{2}\sum_{n_i \neq n_s}\frac{\left(\langle x\rangle_{n_i n_s}^2\right)^2}{(n_s - n_i)^2}\,f_{n_i m}^{(0)}(x)\right]. \tag{5}$$

Evidently, the first-order correction to the total wave function (2) is expressed in the form

$$\psi_{n_1 n_2 m}^{(1)} = \sqrt{2}\,\varepsilon^{3/2}\left[f_{n_1 m}^{(1)}(\varepsilon\xi) f_{n_2 m}^{(0)}(\varepsilon\eta) + f_{n_1 m}^{(0)}(\varepsilon\xi) f_{n_2 m}^{(1)}(\varepsilon\eta)\right] \times \frac{\exp(\mathrm{i}m\varphi)}{\sqrt{2\pi}}\,, \tag{6}$$

and the second-order correction is given by

$$\psi_{n_1 n_2 m}^{(2)} = \sqrt{2}\,\varepsilon^{3/2}\left[f_{n_1 m}^{(2)}(\varepsilon\xi) f_{n_2 m}^{(0)}(\varepsilon\eta) + f_{n_1 m}^{(1)}(\varepsilon\xi) f_{n_2 m}^{(1)}(\varepsilon\eta) + f_{n_1 m}^{(0)}(\varepsilon\xi) f_{n_2 m}^{(2)}(\varepsilon\eta)\right]\frac{\exp(\mathrm{i}m\varphi)}{\sqrt{2\pi}}\,. \tag{7}$$

We are actually interested in the behavior of the wave functions perturbed by the laser field in the spherical coordinates near zero. Small r correspond to small ξ and η, so that functions $f_{n_1 m}$ and $f_{n_2 m}$ can be expanded into a Taylor series. Pronounced WF polarization by the laser field takes place only for the states with $|m| = 0$.[3] Then, one has

$$\psi_{n_1 n_2 0}^{(1)}(\xi, \eta \sim 0) = \frac{3(n_1 - n_2) n^{1/2} A r_\mathrm{B}^{1/2}}{8\sqrt{\pi}\,Z_\mathrm{eff}^{3/2} e}\,, \tag{8}$$

[3] The action of a uniform constant electric field on single-electron WFs with $m \neq 0$ is different. Because these WFs change signs, besides being nonzero in axially symmetric regions, the zero WF value remains immobile at point $r = 0$. Only the electro-induced change in the coefficient of r in equation (1) takes place for WF with $l = 1$, in the coefficient of r^2 for WF with $l = 2$, etc.

i.e., the first-order correction is proportional to the difference between parabolic quantum numbers; it vanishes when these numbers become equal [26, 27]. Accordingly, the second-order correction to wave function (2), namely

$$\psi_{n_1 n_2 0}^{(2)}(\xi, \eta \sim 0) = \frac{n^{5/2} A^2 r_\mathrm{B}^{5/2}}{8\sqrt{\pi}\,Z_\mathrm{eff}^{9/2} e^2}\left(n_1^3 + n_2^3 - n_1^2 - n_2^2 + 2n_1 + 2n_2 - \frac{3}{2}\right), \tag{9}$$

does not vanish even at equal parabolic quantum numbers.

Let us turn now to the calculation of the WF in a laser field. Because the exact hydrogen-like WFs in the spherical coordinates are the linear combinations of the WFs in the parabolic coordinates [26], then it follows:

$$\psi_{2,1,0}(r, \theta, 0) = \frac{1}{2\sqrt{2}}\left[\psi_{1,0,0}(\xi, \eta) - \psi_{0,1,0}(\xi, \eta)\right], \tag{10}$$

$$\psi_{3,2,0}(r, \theta, 0) = \frac{1}{2\sqrt{3}}\left[\psi_{2,0,0}(\xi, \eta) + \psi_{0,2,0}(\xi, \eta) - 2\psi_{1,1,0}(\xi, \eta)\right]. \tag{11}$$

The substitution of formula (8) into formula (10) shows that even the first-order correction to the first WF at zero point does not equal zero, and

$$\psi_{2,1,0}(r \to 0, \theta, \varphi) \simeq \frac{Z_\mathrm{eff}^{5/2}}{4\sqrt{2\pi}\,r_\mathrm{B}^{5/2}}\,r\cos\theta + \frac{3A\sqrt{3r_\mathrm{B}}}{8\sqrt{\pi}\,Z_\mathrm{eff}^{3/2} e}\cos(\theta - \gamma)\,, \tag{12}$$

where γ is the angle between the direction of the laser electric field and the WF polar angle, and $Z_\mathrm{eff} = Z_{\mathrm{L_{III}}}$. The analogous calculation of the first-order correction to the second WF at zero point yields its zero value and necessitates taking account now of the second-order correction. Thus, one obtains

$$\psi_{3,2,0}(r \to 0, \theta, \varphi) \simeq \frac{\sqrt{3}\,Z_\mathrm{eff}^{7/2}}{324\sqrt{2\pi}\,r_\mathrm{B}^{7/2}}\,r^2\left(\cos^2\theta - \frac{1}{3}\right) + \frac{9\sqrt{3}\,A^2 r_\mathrm{B}^{5/2}}{2\sqrt{\pi}\,Z_\mathrm{eff}^{9/2} e^2}\left[\cos^2(\theta - \gamma) - \frac{1}{3}\right]^2. \tag{13}$$

Here, $Z_\mathrm{eff} = Z_{\mathrm{M_V}}$. For the third-order forbidden capture of electrons, the third-order correction to the wave function $\psi_{4,3,0}(r \to 0, \theta, \varphi)$ needs to be calculated.

As mentioned above, the electron capture acceleration factor α can be found from the absolute values squared of wave functions (12), (13) averaged over time and the orientation of the laser electric field vector and integrated over the nucleus volume. The quantity thus obtained must then be carried over to the integral of unperturbed WFs over the nucleus volume. Of special interest are large α, at which the WF polarization shift markedly exceeds r_n. Thus, for the first-forbidden electron capture, one finds

$$\alpha_1 = \alpha_{\mathrm{L_{III}}} \approx \frac{25}{4Z_{\mathrm{L_{III}}}^8}\left(\frac{r_\mathrm{B}}{r_\mathrm{n}}\right)^2\frac{I_{l0}}{I_0}\,. \tag{14}$$

The acceleration factor ($I_{l0} = cA^2/8\pi$) of the second-forbidden electron capture under analogous conditions is given by

$$\alpha_2 = \alpha_{\mathrm{M_V}} \approx \frac{3^{15}\pi}{8Z_{\mathrm{L_{III}}}^{16}}\left(\frac{r_\mathrm{B}}{r_\mathrm{n}}\right)^4\frac{I_{l0}^2}{I_0^2}\,. \tag{15}$$

Let us consider concrete examples. The decay of a long-lived lead isotope (with a half-life of 1.53×10^7 years) $^{205}\mathrm{Pb} \to {}^{205}\mathrm{Tl}$ proceeds with a change in the total nuclear momentum by 2 and a change in parity. This is the unique first-order forbidden capture of electrons. The acceleration $\alpha_1 \simeq 1.7 \times 10^{-6}\, I_{l0}/I_0$. A laser radiation fluence of $\sim 6 \times 10^6\, I_0 \sim 10^{23}$ W cm^{-2} is needed for the appreciable ($\alpha_1 \sim 10$) acceleration of this capture. Such fluences remain to be reached. Another example of a similar process is the capture of electrons in a long-lived $^{81}\mathrm{Kr}$ isotope (with a half-life of 2.29×10^5 years [17]). For $^{81}\mathrm{Kr} \to {}^{81}\mathrm{Br}$ decay, $\alpha_1 \simeq 0.35\, I_{l0}/I_0$. A tenfold acceleration is already achieved at fluences $I_{l0} \sim 10^{18}$ W cm^{-2}.

The possibility of the experimental observation of acceleration of the second-order forbidden capture in the laser field is much more obvious: the effective charge is lower, and polarizability higher. The second-order forbidden electron capture, e.g., in a $^{133}\mathrm{Ba}$ isotope (with a half-life of 10.51 years), $^{133}\mathrm{Ba} \to {}^{133}\mathrm{Cs}$, is characterized by $\alpha_2 \simeq 300\,(I_{l0}/I_0)^2$, i.e., $\alpha_2 \sim 10$ at $I_{l0} \sim 10^{16}$ W cm^{-2}.

It is especially interesting to consider processes involving stable nuclei. For the second-order forbidden electron capture $^{123}\mathrm{Te} \to {}^{123}\mathrm{Sb}$, $\alpha_2 \simeq 1000(I_{l0}/I_0)^2$, i.e., $\alpha_2 \sim 10$ at $I_{l0} \sim 10^{15}$ W cm^{-2}. This process has until recently been interpreted as a K-capture, in conformity with the emission of quantum with the energy in the 28-keV region — the K_α-line of $^{123}\mathrm{Sb}$ with a lifetime exceeding 10^{13} years [28]. The same value was collated in tables [17]. However, later (more accurate) studies demonstrated that there is no such emission, and the $^{123}\mathrm{Te} \to {}^{123}\mathrm{Sb}$ decay cannot be interpreted as K-capture [29]. The half-life was shown to be constrained by the value of $t_{1/2} > 9.2 \times 10^{16}$ years [29].

4. Possibilities of experimental realization

The intensities of laser radiation needed to accelerate the first-forbidden electron capture are rather high: at present, they are realized in short (less than 1 ps) superpower laser pulses with a low repetition rate. Nevertheless, amplification of characteristic X-ray radiation with transitions from the L_{III}-shell is possible to observe even if in the X-ray photon counting mode. The process of electron capture acceleration is likely to be accompanied by marked ionization of the atoms being studied.

The acceleration of the second-forbidden electron capture is easier to realize. The necessary radiation intensities can be reached even by focusing powerful radiation of continuous wave lasers. In order to prevent the formation of highly ionized plasma, the experiment may consist in focusing laser radiation into strongly rarefied atomic vapor 'clouds'. The rather small total number of 'working' nuclei is compensated for by the continuity of laser irradiation. We note that many interesting nuclei, first and foremost light ones, remain beyond the framework of the approximation. By way of example, it can be expected that a 10-fold acceleration of electron capture in $^{54}\mathrm{Mn} \to {}^{54}\mathrm{Cr}$ ($t_{1/2} = 312$ days)[4] will be possible to achieve at a laser radiation intensity of $\sim 10^{11} - 10^{12}$ W cm^{-2}. The experiment can be conducted by the irradiation of a solid state target with a large number of decaying nuclei. The conditions for the third-forbidden electron capture are even more readily available [30].

5. Acceleration of neutrinoless double capture of orbital electrons

Here are some physical considerations as regards the possibility of achieving acceleration of significant (thus far hypothetical) neutrinoless double capture of orbital electrons by stable nuclei through the application of a strong electric field (including a laser field) to the atoms. Such a process, hypothesized as early as 1955 [31], can be realized if a neutrino coincides with its antiparticle (E Majorana's hypothesis). In such a case, two consecutive electron capture processes need to be summarized for a nucleus of mass number $A + 2$:

$$\begin{aligned}&\left[(A+2) + \mathrm{e} \to (A+1) + \nu_\mathrm{e}\right] \\ &\quad + \left[(A+1) + \mathrm{e} + \bar{\nu}_\mathrm{e} \to A + \gamma\right] \\ &\quad = (A+2) + 2\mathrm{e} \to A + \gamma\,. \end{aligned} \tag{16}$$

Formally, in this case the neutrino of the first process and the antineutrino of the second one cancel each other out (physically, the neutrino is emitted in the former process, and absorbed in the latter). The two events are integrated into the resultant process with the emission of a gamma quantum. Such transitions occur between nuclei $0^+ \to 0^+$; there are a total of 12 such pairs with pure electron capture without positron emission [17].

Evidently, the time between the first process and the second one is not too large: it is at least shorter than the neutrino time of flight in the nucleus of interest, and the distance travelled by the neutrino is shorter than the nuclear radius. This fact accounts for the magnitude of the nuclear transition matrix element between the parent $(A + 2)$ and daughter (A) nuclei: it appears to be lower for transitions with a smaller intermediate nuclear momentum. Indeed, the uncertainty relation for the angle φ and angular momentum L_z is written as [23, 24]

$$\left\langle (\Delta L_z)^2 \right\rangle \left\langle (\Delta\varphi)^2 \right\rangle \geqslant \frac{\hbar^2}{4}\,,$$

and at small angular displacements $\Delta\varphi$ (the spatial displacements of protons that capture an electron inside the nucleus being small, too) it determines the rather large values of ΔL_z associated with the first capture, i.e., in the intermediate $(A + 1)$ nucleus. For this reason, the above-mentioned nuclear matrix element must be larger (much larger) for such neutrinoless double captures in which electron capture by the intermediate nucleus is forbidden. It is clear, however, that the wave function of the electron being captured at the nucleus is smaller (by a factor of $Z_{\mathrm{eff}} r_\mathrm{n}/r_\mathrm{B}$ to the appropriate power), and the result for the double forbidden and allowed capture rates is roughly equal (in any case, the difference will not be as great as for single-electron captures [20, 25]). When the wave function of the captured electron with the nonzero orbital quantum number is shifted by an electric field with respect to the nucleus, the amplitude of this function at the nucleus increases, which leads to the acceleration of the double electron capture. In transitions between nuclei $0^+ \to 0^+$, the acceleration factor is simply the corresponding acceleration factor squared of the forbidden single-electron capture (14), (15).

[4] Breakdown voltage of pure Mn salts amounting to 10^9 W cm^{-1} (such a field amplitude corresponds to a radiation intensity of 10^{15} W cm^{-2}), the experiment can be conducted by placing a sample of such salt in a constant electric field of ~ 10 MV cm^{-1}.

6. Neutrinoless double capture to the resonance states of daughter nuclei and possibilities of its experimental realization

The 'surplus' energy in neutrinoless double electron capture must be eliminated by a γ-quantum with the appropriate energy. If the daughter nucleus lacks resonance levels in close proximity to the ground state (minus the binding energy of the electrons being captured), the main process by which such γ-quanta are generated in the parent nucleus is bremsstrahlung [32]. The presence of such closely spaced excited levels would sharply increase the probability of double capture, because it might occur to the resonance state with a subsequent resonant release of the corresponding γ-quantum. The calculation of such resonant processes for certain nuclei is reported in Refs [33–36]; it is proposed to employ synchrotron radiation to realize induced transitions to the excited state of the daughter nucleus [37]. The resonance parameter F in the probability of double capture to the excited state has the form [38]

$$F = \frac{\Gamma_{2h}}{\Delta^2 + \Gamma_{2h}^2/4}\,, \tag{17}$$

where $\Delta = Q - B_{2h} - E_\gamma$, B_{2h} and Γ_{2h} are the energy and the width, respectively, of a double electron hole in the atomic electron shell of the daughter nucleus, Q is the difference between the binding energies of the parent and daughter nuclei, and E_γ is the energy of the excited level in the daughter nucleus.

Isotope ^{74}Se possesses the lowest Δ among known nuclei: for electron capture from L_{III} and L_I shells, $\Delta_{Se} = 2.6$ keV (the data of Ref. [33]; the value of Q for a $^{74}\text{Se} \to {}^{74}\text{Ge}$ pair was measured to an accuracy of 2.3 keV [33]). Initially, the first-forbidden capture to the virtual ^{74}As nucleus ground state 2^- occurs; it is followed by the allowed capture to the excited state 2^+ of ^{74}Se. According to Ref. [33], the upper estimate of the half-life at such a mismatch Δ_{Se} (in the first capture from the L_{II} but not the L_{III} shell) amounts to 0.55×10^{19} years. The above reasoning leads to the conclusion that the double electron capture from the L_{III} and L_I shells must be faster.

In the course of atomic ionization, the absolute value of the electron binding energy in the remaining shells becomes higher, because nucleus shielding weakens. Moreover, the ionization energy during transition between electron shells undergoes a strong jump (the ionization energy of neonlike Se^{24+} is 2542 eV compared with 1036.3 eV in the preceding Se^{23+} ion). This fact was utilized, for instance, in designing plasma X-ray lasers [39, 40]. The electron binding energy in the L_{III} shell of neonlike $^{74}Se^{24+}$ roughly equals the ionization energy, 2542 eV; it is 15% higher or 2923 eV (as in the initial atom [41]) in the L_I shell. Thus, $B_{2h}^i \approx 5.5$ keV in an $^{74}Se^{24+}$ ion, i.e., $\Delta_{Se}^i \approx 0$! (see Fig. 1), which means that the value of Δ_{Se}^i for the $^{74}Se^{24+}$ ion is on the order of several dozen electron-volts. The value of Γ_{2h}^i in the $^{74}Se^{24+}$ ion being also different (1.5 times higher) from the atomic value of Γ_{2h}, this fact should be taken into account in the acceleration factor.

Thus, we have to deal with two acceleration factors of neutrinoless double capture of electrons from the L_{III} and L_I shells of ^{74}Se in a strong laser field. The strongest of them is bringing quantity (17) into resonance as a result of the Stark shift of the inner electron energy levels in the ion as compared with those in the atom. In this case, the acceleration of the first-forbidden capture from the L_{III} shell to a virtual nucleus [in the absence of acceleration of the capture from the L_I shell (see above)] is not too high. The resultant acceleration factor α_1^{res} can be obtained by multiplying the resonance factor ratio (17) for the ion and atom by α_1. In this case, if

$$\frac{25}{4Z_{L_{III}}^8}\left(\frac{r_B}{r_n}\right)^2 \frac{I_{l0}}{I_0} > 1\,,$$

then

$$\alpha_1^{res} \approx \frac{25}{4Z_{L_{III}}^8}\left(\frac{r_B}{r_n}\right)^2 \frac{I_{l0}}{I_0}\,\frac{\Delta^2\Gamma_{2h}^i}{(\Delta^i)^2\Gamma_{2h}}\,; \tag{18a}$$

in the opposite case, one finds

$$\alpha_1^{res} \approx \frac{\Delta^2\Gamma_{2h}^i}{(\Delta^i)^2\Gamma_{2h}}\,. \tag{18b}$$

Substituting parameters of the ^{74}Se L_{III} and L_I shells and $\Gamma_{2h} \sim 1$ eV, and taking for once into consideration the absence of acceleration of electron capture from the L_{III} shell (the intensity of the laser field is sufficient to maintain only a plasma with ions of the desired degree of ionization and case (18b) is realized), we arrive at $\alpha_1^{res} \sim 10^4$ and, therefore, the time of such a process in the laser field of the specified intensity covers $\sim 5 \times 10^{14}$ years).

The maintenance of dense, hot $^{74}Se^{24+}$ plasma can be achieved in different ways [39, 40]. One can confine it in a trap created by pulsed beams of one or several CO_2 lasers (see Refs [42, 43] for the description of traps). When a system of laser beams [42, 43] keeps the number of ions relevant to 1 g of ^{74}Se, the minimum time of an experiment needed to detect γ-quanta with energies 608.35 and 595.85 keV from an emitting ^{74}Ge nucleus may be as short as a few seconds.

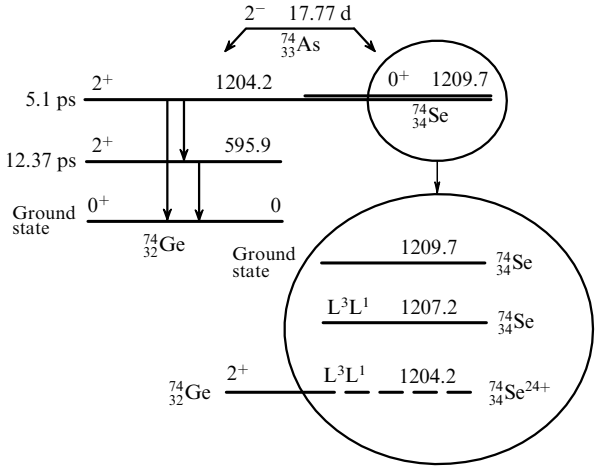

Figure 1. Schematic of energy layers in the neutrinoless electron capture $^{74}\text{Se} \to {}^{74}\text{Ge}$. Left: lower excited levels of ^{74}Ge and the corresponding lifetimes. The ellipse encompasses energy levels of the ^{74}Se ground state, double holes in the L_I and L_{III} electron shells of a ^{74}Se atom, and a neonlike $^{74}Se^{24+}$ ion. The $1204.2 \to$ ground state transition in ^{74}Ge is roughly half as probable as the $1204.2 \to 595.9$ transition [13] (all energies are expressed in kiloelectron-volts).

7. Conclusion

The intensities of laser radiation needed to accelerate the first-forbidden electron capture by nuclei are relatively high: at present, they are realized in short superpower laser pulses less than 1 ps in duration at a low repetition rate. Nevertheless,

observation of the acceleration of characteristic X-ray radiation with transitions from the L_{III} electron shell appears possible even if in the X-ray photon counting mode.

Acceleration of the second-forbidden capture is easier to realize. The necessary intensities of laser radiation can be achieved even by focusing radiation from powerful continuous wave lasers. Equally possible are experiments in a constant electric field of 10–100 MV cm^{-1}, i.e., in a field lower than the breakdown field voltage of many pure dielectrics containing nuclei of interest.

Finally, considerable acceleration of the neutrinoless double capture of electrons, as well as verification of Majorana's hypothesis for the nature of neutrino, is possible in an experiment with a plasma consisting of electrons and neonlike $^{74}Se^{24+}$ ions. Also, the use of heavy ^{168}Yb ions offers great prospects.

The work was supported by a grant from the A von Humboldt Foundation and the program of RAS.

References

1. Nikishov A I, Ritus V I *Zh. Eksp. Teor. Fiz.* **46** 1768 (1964) [*Sov. Phys. JETP* **19** 1191 (1964)]
2. Ritus V I *Zh. Eksp. Teor. Fiz.* **56** 986 (1969) [*Sov. Phys. JETP* **29** 532 (1969)]
3. Ternov I M et al. *Pis'ma Zh. Eksp. Teor. Fiz.* **37** 288 (1983) [*JETP Lett.* **37** 342 (1983)]
4. Ternov I M, Rodionov V N, Dorofeev O F *Zh. Eksp. Teor. Fiz.* **84** 1225 (1983) [*Sov. Phys. JETP* **57** 710 (1983)]
5. Akhmedov E Kh *Zh. Eksp. Teor. Fiz.* **85** 1521 (1983) [*Sov. Phys. JETP* **58** 883 (1983)]
6. Nikishov A I, Ritus V I *Zh. Eksp. Teor. Fiz.* **85** 24 (1983) [*Sov. Phys. JETP* **58** 14 (1983)]
7. Becker W, Schlicher R R, Scully M O *Nucl. Phys. A* **426** 125 (1984)
8. Ray A et al. *Phys. Rev. C* **66** 012501(R) (2002)
9. Kusaba M et al., Annu. Rept. Jan. – Dec. 1989 (Tokyo: Inst. Nucl. Study Univ. Tokyo, 1990)
10. Emery G T *Annu. Rev. Nucl. Sci.* **22** 165 (1972)
11. Morita M *Prog. Theor. Phys.* **49** 1574 (1973)
12. Ivanov L N, Letokhov V S *Zh. Eksp. Teor. Fiz.* **68** 1748 (1975) [*Sov. Phys. JETP* **41** 877 (1975)]
13. Ivanov L N, Letokhov V S *Zh. Eksp. Teor. Fiz.* **93** 396 (1987) [*Sov. Phys. JETP* **66** 227 (1987)]
14. Letokhov V S *Opt. Commun.* **106** 227 (1994)
15. Pontecorvo B, Kirkwood D H W, Hanna G C *Phys. Rev.* **75** 982 (1949)
16. Hubbard W M *Phys. Rev.* **137** B245 (1965)
17. Firestone R B, Baglin C M, Chu S Y F (Eds) *Table of Isotopes* (New York: Wiley, 1999)
18. Wing J, Stevens C M, Huizenga J R *Phys. Rev.* **111** 590 (1958)
19. Hopke P K, Naumann R A *Phys. Rev. C* **4** 606 (1971)
20. Dzhelepov B S, Zyryanova L N, Suslov Yu P *Beta-Protsessy. Funktsii dlya Analiza Beta-Spektrov i Elektronnogo Zakhvata* (Beta Processes. Functions for the Analysis of Beta-Spectra and Electron Capture) (Leningrad: Nauka, 1972)
21. Zener C *Phys. Rev.* **36** 51 (1930)
22. Slater J C *Phys. Rev.* **36** 57 (1930)
23. Landau L D, Lifshitz E M *Kvantovaya Mekhanika. Nerelyativistskaya Teoriya* (Quantum Mechanics. Non-Relativistic Theory) 2nd ed. (Moscow: Fizmatgiz, 1963) [Translated into English (Oxford: Pergamon Press, 1977)]
24. Davydov A S *Kvantovaya Mekhanika* (Quantum Mechanics) 2nd ed. (Moscow: Nauka, 1973) [Translated into English (Oxford: Pergamon Press, 1976)]
25. Wapstra A H, Nijgh G J, Van Lieshout R *Nuclear Spectroscopy Tables* (Amsterdam: North-Holland, 1959) [Translated into Russian (Moscow: Gosatomizdat, 1960)]
26. Bethe H A, Salpeter E E *Quantum Mechanics of One- and Two-Electron Atoms* (Berlin: Springer, 1957) [Translated into Russian (Moscow: Fizmatgiz, 1960)]
27. Elyutin P V, Krivchenkov V D *Kvantovaya Mekhanika s Zadachami* (Quantum Mechanics with Problems) 2nd ed. (Moscow: Fizmatlit, 2001)
28. Watt D T, Glover R N *Philos. Mag.* **7** 105 (1962)
29. Alessandrello A et al. *Phys. Rev. C* **67** 014323 (2003)
30. Romanovskii M Yu *Pis'ma Zh. Eksp. Teor. Fiz.* **94** 460 (2011) [*JETP Lett.* **94** 425 (2011)]
31. Winter R G *Phys. Rev.* **100** 142 (1955)
32. Sujkowski Z, Wycech S *Phys. Rev. C* **70** 052501(R) (2004)
33. Barabash A S et al. *Nucl. Phys. A* **785** 371 (2007)
34. Vergados J D *Phys. Rev. C* **84** 044328 (2011)
35. Eliseev S et al. *Phys. Rev. C* **83** 038501 (2011)
36. Eliseev S et al. *Phys. Rev. C* **84** 012501(R) (2011)
37. Goncharov M *Phys. Rev. C* **84** 028501 (2011)
38. Bernabeu J, De Rujula A, Jarlskog C *Nucl. Phys. B* **223** 15 (1983)
39. Matthews D L et al. *Phys. Rev. Lett.* **54** 110 (1985)
40. MacGowan B J *J. Appl. Phys.* **61** 5243 (1987)
41. Grigoriev I S, Meilikhov E Z (Eds) *Fizicheskie Velichiny* (Handbook of Physical Quantities) (Moscow: Energoatomizdat, 1991) [Translated into English (Boca Raton, NY: CRC Press, 1996)]
42. Korobkin V V, Romanovsky M Yu *Phys. Rev. E* **49** 2316 (1994)
43. Korobkin V V, Romanovsky M Yu *Laser Part. Beams* **16** 235 (1998)

PACS numbers: **02.70.–c**, **05.10.–a**, **05.50.+q**
DOI: 10.3367/UFNe.0182.201207j.0787

Computational physics and testing theoretical predictions

L N Shchur

1. Introduction

Computational physics was born simultaneously with the creation of the first electronic computers.[1] Physicists used computers to achieve a practical goal important at that moment: to develop thermonuclear weapons. One of the first computational tasks needed for peaceful applications was the work of Fermi, Pasta, and Ulam [1] on simulating the dynamics of the one-dimensional nonlinear chain; the work was done on the MANIAC 1 mainframe computer in Los Alamos [2]. The opinion prevalent at the beginning of the 1950s was that nonlinearity should lead to equipartition of energy over degrees of freedom, i.e., to stochastization. Contrary to expectations, numerical experiments revealed quasiperiodic behavior. This phenomenon was explained in 1965 by Zabusky and Kruskal [3], who numerically identified solitons (and introduced the very term 'soliton') and found their inelastic scattering. This result led to the discovery of the inverse scattering problem method [4] which, in turn, became the key to obtaining exact solutions of nonlinear problems (see, e.g., monograph [5]). This is an impressive example of the

[1] The author uses the Russian term 'electronic computing machine' (EVM in *Russ. abbr.*) interchangeably with the currently widespread term 'computer' in those section of the text where it was historically justifiable. The English translation uses the term 'computer' throughout.

L N Shchur L D Landau Institute for Theoretical Physics, Russian Academy of Sciences, Chernogolovka, Moscow region, Russian Federation
E-mail: lev@landau.ac.ru

Uspekhi Fizicheskikh Nauk **182** (7) 787 – 792 (2012)
DOI: 10.3367/UFNr.0182.201207j.0787
Translated by V I Kisin; edited by A Radzig

success of computational physics and, in particular, of the computational experiment — the first case of a numerical experiment generating new knowledge.

Another important method created at about the same time was the Monte Carlo method developed by Metropolis in collaboration with Rosenbluth and Teller for modeling thermodynamic phenomena [6]. The Monte Carlo method lies at the basis of virtually the entire current research in computational statistical physics.

The distinguishing characteristic of computational physics consists in using computers for the study of physical phenomena. Important aspects of the successful application of computers are the algorithms and methods of calculation and simulation, as well as methods of processing the results obtained, thereby extracting new knowledge.

This report presents the author's experience in applying the methods of computational physics to testing theoretical predictions and hypotheses. As an illustration we have selected several specific examples of solving problems of nonlinear physics and statistical mechanics; they develop and demonstrate the current status of these historically first fields to which computational physics was applied.

2. Testing integrability of nonlinear models

In the 1960s–1980s, progress in the inverse scattering problem method led to explosive growth in the number of exactly solved models of theoretical and mathematical physics. For example, attempts were made to exactly solve equations of two-dimensional hydrodynamics, Yang–Mills equations, cosmological problems, and some others. Applications of computational physics can suggest arguments in favor of the integrability of the model or give a definite conclusion of nonintegrability of the model in question, and in some cases achieve results at the level of a 'computer-assisted proof', i.e., the level of rigorousness of a theorem.

2.1 Nonintegrability of two-dimensional hydrodynamics

There is an elegant reply to the question about integrability of two-dimensional hydrodynamics [7]. The energy of a two-dimensional vortex diverges logarithmically. Let us compose a pair of vortices with different signs but equal absolute vorticity κ. The energy of this vortex pair is finite, and its momentum (both projections) is conserved, i.e., a vortex pair exhibits the properties of a particle. This particle is not at rest and, when alone, it moves along a straight line with the constant velocity $v = \kappa/a$, where a is the distance between the vortices. We can analyze numerically the problem of scattering of vortex particles with vorticities κ and $\kappa + \epsilon$ ($\epsilon \ll \kappa$) on one another. The resulting dependence of the scattering angle on the impact parameter is irregular, with accumulation points presenting. The lifetime of the captured state, in which all four vortices are at a finite distance from each other on the order of $\kappa a/\epsilon$, increases in the vicinity of these accumulation points. The divergence of the capture time is analogous to the known phenomenon of the capture of three bodies in celestial mechanics; its nonintegrability was proved by Poincaré [8]. The hope that additional integrals of motion exist in the scattering of vortex pairs (in addition to the above-mentioned energy and momenta) is incompatible with the phenomenon of stochasticity of their scattering. Notice that paper [7] appears to be the first ever computational work on stochastic scattering.

2.2 Nonintegrability of the classical Yang–Mills fields

The problem of integrability of classical Yang–Mills fields, in particular via the numerical solution of equations, was formulated by V E Zakharov and was widely discussed in the scientific literature. An unambiguous answer to the question was obtained in paper [9]. The original Yang–Mills equations can be reduced by an admissible substitution to a dynamical system described by a Hamiltonian with two degrees of freedom. The phase space of the dynamical system $(x, \dot{x}, y, \dot{y})$, where (x, y) are two coordinates, and $(\dot{x}, \dot{y})$ are the corresponding momenta, is four-dimensional. The fixed value of the energy integral $E = -(1/2)\{\dot{x}^2 + \dot{y}^2 + x^2y^2\} = \text{const}$ defines a three-dimensional hypersurface in four-dimensional space. The phase portrait of the system is now numerically constructed in the Poincaré cross section, i.e., the cross section of the three-dimensional hypersurface by the half-plane $y = 0$, $\dot{y} > 0$. If an additional integral of motion I_1 existed, the initial values would fix the value of the integral $I_1 = \text{const}$ and the points of the Poincaré cross section would be isolated or would lie in closed curves defined by this value $I_1 = \text{const}$. Numerical analysis established that invariant curves (or separatrices) of the fixed points intersect at a nonzero angle. For example, trivial periodic solutions $x = y = +F$ and $x = y = -F$, where $F = \text{cn}\,(t, 1/\sqrt{2}\,)$ is the Jacobi elliptic cosine, correspond to fixed points in the Poincaré cross section with coordinates $(0; 1/\sqrt{2}\,)$ and $(0; -1/\sqrt{2}\,)$. The linearized Poincaré map in the vicinity of these points is hyperbolic, and its eigenvalues are $\lambda_1 = 129{,}647014\ldots$ and $\lambda_2 = 1/\lambda_1$. The numerically constructed separatrices of these points intersect at an angle of about 72°. Under the conditions of the numerical calculations, the obtained value of the angle greatly exceeds possible calculation errors. This constitutes the proof of the nonintegrability of Yang–Mills equations in the style of the computer-assisted proof.

2.3 The exact solution of the interchange of Kasner epochs

The next example belongs to the study of statistical properties of the oscillatory evolution [10] of homogeneous cosmological vacuum Bianchi Type-IX models [11]. The duration n of the epoch is measured in the number of oscillations k_n of the epoch. The infinite sequence k_n ($n = 0, 1, 2, \ldots$) is determined by the numbers $x_{-1}, x_0, x_1, x_2, \ldots$ ($0 < x_s < 1$) related to one another by the transformation $x_{s+1} = \{1/x_s\}$, where the braces stand for the fractional part of a number. Note that the durations (lengths) are $k_s = [1/x_{s-1}]$, where the brackets denote the integer part of a number. We can write down an expression for x_s in terms of k_s as a continued fraction $x_{s-1} = 1/(k_s + 1/(k_{s+1} + 1/(k_{s+2} + \ldots \equiv x_s^+$. This law of interchange of epoch lengths results in stochastization of the behavior of the model as it evolves to a singularity. The probability density distribution on the segment $(0, 1)$ of the values $x_s \equiv x$ is given by the Gauss formula $w(x) = 1/(1 + x)\ln 2$. Let us denote the moment when the sth epoch begins by Ω_s; we can now derive the following recurrence formulae relating the characteristics of the two successive epochs:

$$\frac{\Omega_{s+1}}{\Omega_s} = 1 + \delta_s k_s \left(k_s + x_s + \frac{1}{x_s} \right),$$

$$\frac{\delta_{s+1}}{\delta_s} = 1 - \frac{k_s/x_s + 1}{\Omega_{s+1}/\Omega_s}\,.$$

Numerical solution of these equations [12] showed that the quantity $\delta_s \equiv \delta$ has a stable distribution $P(\delta)$ whose plot is approximated well by the function

$$P(\delta) = 1\big(|1 - 2\delta| + 1\big) \ln 2 \,.$$

Analytical studies gave evidence that the problem can be solved by the introduction of a continued fraction with a reverse sequence of denominators

$$x_s^- = 1/(k_{s-1} + 1/(k_{s-2} + 1/(k_{s-3} + \dots \,.$$

It turns out that the joint probability distribution for x_s^+ and x_s^- is given by the formula $P(x^+, x^-) = 1/(1 + x^+ x^-)^2 \ln 2$, which provides the exact solution to the initial problem and confirms that the approximating function given above comprises a solution of the problem, and that it is the exact solution.

This example is significant in that a carefully worked out solution of the problem may lead to discovering the exact result [12]. In its time, it has greatly changed the attitude of theoreticians to work on computational physics.

3. Monte Carlo methods

We have mentioned in the Introduction that, already at the dawn of the computer era, the Monte Carlo method was developed for solving problems of statistical physics. The name itself indicates that the method leans upon randomness (e.g., in choosing values of a random variable from a specific distribution). Computers follow strictly deterministic algorithms, so that randomness cannot be achieved in the course of executing a program. Two approaches appear inescapable, and both have been used ever since the first days of computers: an algorithmic approach to generating a pseudorandom sequence, and an approach using an external source of real noise. In the former, researchers initially applied the middle-square method proposed by J von Neumann. An integer of n bits is squared. This generally gives $2n$ bits, of which the left- and rightmost $n/2$ bits are dropped, while the middle n bits are used as the next pseudorandom number. It was understood rather soon that this method does not generate a sequence that meets the requirements of intuitively expected randomness. In essence, the algorithms for generating random numbers define a mapping of a certain number of equally spaced points of a unit segment onto itself. In other words, the algorithm for generating random numbers is equivalent to a dynamical system in the set of rational numbers of the unit segment. Keeping in mind the lesson of the first computational experiment by Fermi, Pasta, and Ulam on stochastization, one should not be surprized by the fact that the development of algorithmic methods for generating pseudorandom numbers is a serious scientific issue requiring special attention. We shall not engage in a discussion of this largely mathematical problem in this report, referring the reader to detailed discussions of the issue in our papers [13–15]. The second method consists in using a device in which the generation of randomness is based on a physical principle. For instance, a method has recently been proposed to digitize the fluctuating intensity of a chaotic semiconductor laser [16].

In this section, we turn our attention to methods of numerical analysis of models in statistical physics. The main purpose of this analysis is to test theoretical hypotheses and predictions.

3.1 Two-dimensional Ising model with impurities

The effect of impurities on the critical behavior of systems is one of the most interesting features, from both the theoretical and the practical points of view. The critical behavior of the two-dimensional Ising model was studied exactly by Onsager in one of the most beautiful theoretical works [17], published in 1944. At the beginning of the 1980s, the brothers Vladimir and Victor Dotsenko found that the critical behavior of specific heat is modified by a logarithmic correction [18]. Their theory was for a long time the object of intense discussions, with conflicting claims. It was decided to carry out extensive numerical studies.

3.2 Dedicated SPP-1 and SPP-2 processors

In the 1980s, the computational power of supercomputers was insufficient for the numerical study of the fine points of the logarithmic behavior. A group of researchers at the L D Landau Institute for Theoretical Physics (ITF) designed two dedicated processors to attack the problem which presented huge difficulties at the time.

In 1990, they built a processor [19] implementing the Monte Carlo method with Metropolis's algorithm [6] and a pseudorandom number generator of the shift register R250 type [20]. The researchers applied the method of programming with a soldering iron. The algorithm was analyzed and formulated in the form of logical operations with integers and with WRITE and READ memory operations. It was in the end possible to create a computer with an architecture of ideal performance characteristics — all the operations of one Monte Carlo step were performed in one memory cycle. As a result, the performance of the system exceeded that of the Cray 1 supercomputer. Alas, methodological mistakes caused by the order in which generated random numbers were used made it impossible to arrive at any significant results.

In 1994, the second dedicated processor was built [21], which for the first time realized the cluster Monte Carlo method that eliminated the danger of critical slowdown inherent in the Metropolis method. This processor was applied to studying the critical behavior of magnetization, magnetic susceptibility, and specific heat with an accuracy sufficient for reliable confirmation of logarithmic corrections to the three physical quantities mentioned above [22]. The results can be interpreted in the following manner. The correlation length of the pure Ising model, $\xi \propto 1/|\tau|$, where $\tau = (T - T_c)/T$ is the reduced temperature, is modified by impurities in the way that

$$\xi \propto \frac{\sqrt{1 + (4/\pi) g_0 \ln (1/|\tau|)}}{|\tau|} \,.$$

Note that thermodynamic quantities such as magnetization, susceptibility, and specific heat show identical functional dependence on the correlation length both in the pure model and in the impurity model.

Owing to capacity greater than that of the Cray 2 supercomputer, the dedicated processor made it possible for the first time to analyze numerically the correlation function both of pure and impurity Ising models [23], in full agreement with the above interpretation.

The dedicated computer hardware was thus able to successfully conclude the work on the long-standing problem of testing the presence of logarithmic corrections to the thermodynamic functions of the two-dimensional Ising model with impurities.

3.3 The central charge of the Ising model with impurities

Plechko [24] computed the central charge g of the theory for the Ising model with nonmagnetic impurity sites (see also Ref. [25]) as a function of the concentration q of site impurities: $g = 4.843q/(1-q)$. The central charge is included in the dependence of the magnetic susceptibility in the critical region on reduced temperature $\tau = (T - T_c)/T$ as a coefficient of the logarithm:

$$\chi(\tau) = \Gamma|\tau|^{-7/4}(1 + 0{,}07790315\tau)(1 - g\ln|\tau|)^{7/8}\,.$$

Approximating numerical data for the dependence of magnetic susceptibility on temperature by this expression yields the values of two parameters: the amplitude Γ, and the central charge g. The solid curve in Fig. 1 plots the theoretical dependence of the central charge and the results of approximation of the magnetic susceptibility on both sides of the critical point. Both approximations give identical values of the central charge, within computational errors. Both coincide with the theoretical prediction up to the impurity concentration $q \approx 0.1$. This magnitude can be estimated as follows. In addition to the two scales of the pure Ising model, namely the correlation length $\xi \propto 1/|\tau|$ and the size L of the system, the impurity model exhibits two more scales: the mean spacing between impurities $l_i \propto \exp(-1/g)$ [18], and the percolation length $\xi_p \propto (q_c - q)^{4/3}$ [26]. Curiously enough, the last two lengths coincide at $q \approx 0.1$. This can be physically interpreted as indicating that the size of a cluster of nonmagnetic impurities has reached the mean distance between impurities, after which impurities cannot be considered independent, i.e., disorder ceases to be weak.

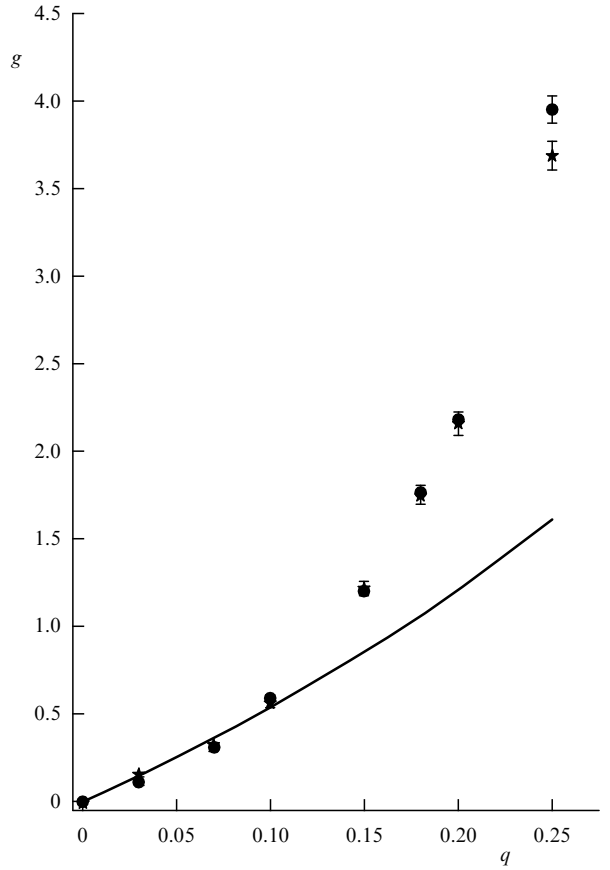

Figure 1. The central charge g as a function of the concentration of site impurities q. The curve traces Plechko's theoretical prediction [24]. Black dots (stars) correspond to an approximation of the numerical data for susceptibility in the low-temperature (high-temperature) field.

3.4 Three-dimensional Ising model and dedicated processors

Attempts to find the exact solution of the three-dimensional Ising model have so far been unsuccessful. This work involves approximate analytical methods and numerical simulation. To test the theoretical hypotheses, one needs to evaluate the critical temperature and critical exponents. Numerical methods for simulation of the three-dimensional Ising model are similar to those discussed above for the two-dimensional model. Evaluation of critical exponents using the renormalization-group methods [27]: $y_t = 1.587(4)$ and $y_h = 2.485(2)$, yields less accurate values than, for example, the values obtained by numerical analysis of high-temperature series [28]; $y_t = 1.5869(4)$ and $y_h = 2.48180(15)$. Early estimates obtained using Monte Carlo techniques [29]: $y_t = 1.590(2)$ and $y_h = 2.482(7)$, yielded rather poor agreement with the predictions of the analytical renormalization group theory.

In the mid-1990s, ITF researchers, together with H Blöte of the University of Delft, developed a cluster processor for studying the three-dimensional Ising model [30]. They implemented the single-cluster Wolff algorithm, which we used successfully in the past to realize a processor for studying the Ising model with impurities [21]. A programmable block was developed to generate random numbers; it allowed us to implement number generator algorithms of the shift register type up to 16,384 in length. Each processor has two such blocks (the two layers at the top left in Fig. 2) which work in parallel, and a random number is obtained by modulo 2 addition. This approach has allowed us to eliminate all reported systematic errors [13, 31]. The spin memory contains 16,777,216 spins, and the boundary conditions are programmable. In all, we manufactured 12 processors controlled by three servers. The accuracy of the numerical estimates achieved with these processors by the Monte Carlo method for the critical temperature of the three-dimensional Ising model, $1/T_c = 0.62358(15)$, and for the values of critical exponents [32] $y_t = 1.5865(14)$ and $y_h = 2.4814(5)$ still remains record-best in the field.

3.5 The critical percolation

In 1995, Aizenman [33] formulated a conjecture at a conference on statistical physics that in the thermodynamic limit the probability of observing two infinite percolating clusters occurring in critical percolation is finite. This inference was counterintuitive. However, numerical simulation gave evidence that this is indeed the case, even though this event is observed very infrequently. For example, out of a thousand square samples of *infinite* linear size, 13 samples, on average, contain two percolating clusters. In a million samples three contained three percolating clusters. We conducted numerical experiments in which a 100 million clusters were generated for each sample size, and analyzed the limiting case of lattices of an infinite size. The resulting numerical estimates were published [34] before John Cardy's analytical solution of the problem became known [35]. The assessments and the analytical solution were found to coincide quite well.

Later simulation of the critical percolation [36] confirmed the complete Aizenman conjecture on the dependence of the

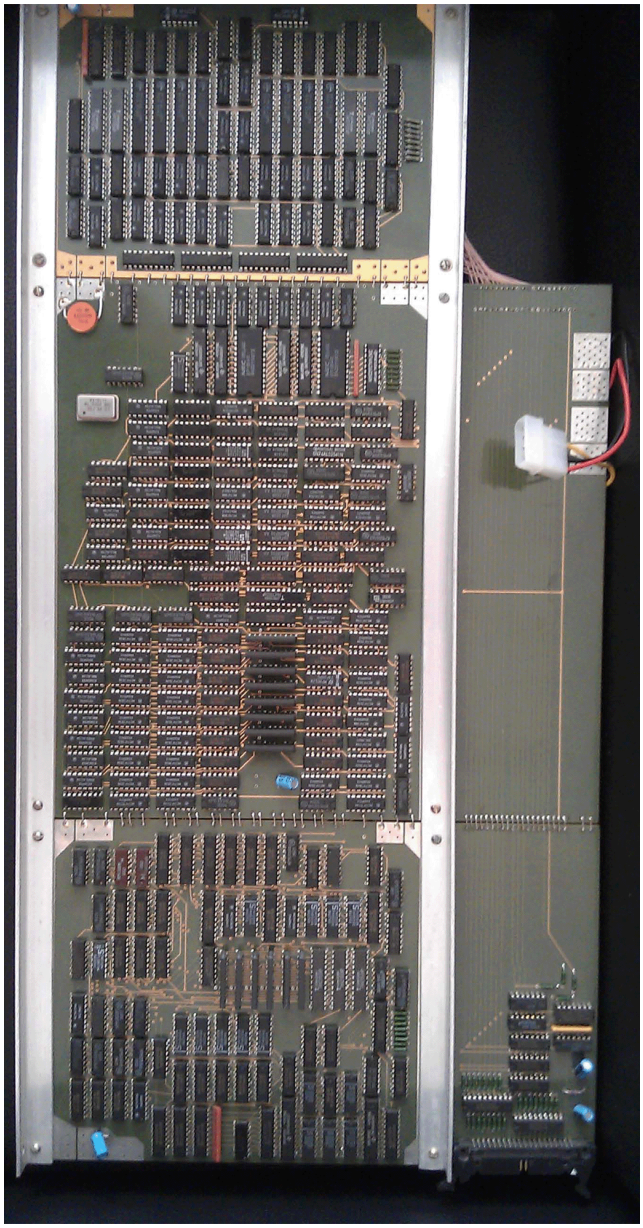

Figure 2. Photograph of the processor board of one of the dedicated processors for the numerical study of the three-dimensional Ising model. From upper left down: random number generator block, single-cluster algorithm block, and spin memory. On the right: I/O block with sockets for connection to server computers.

critical exponent ζ_d of cluster percolation multiplicity on the space dimension $2 < d < 6$: $\zeta_d = d/(d-1)$.

3.6 Duality of critical interfaces

Critical clusters constitute fractal objects [37]. Conformal field theory [38] provides predictions for the critical exponents of two-dimensional objects [39]. Applying this theory, one can compute the fractal dimensions of critical clusters of two-dimensional Potts models, the $O(N)$ model, and some others. The method of analytical calculation of the fractal dimension of boundaries of such clusters (so-called critical interfaces) has been developed fairly recently [40], and accurate results have already been obtained for some models [41]. At the same time, Duplantier [42] advanced a conjecture on the duality of critical interfaces based on some qualitative reasoning and analogies.

Verification of the duality hypothesis for critical interfaces using numerical simulation requires identification of interfaces on the lattice. Analysis of numerical results for Potts models with the number of components from 1 to 4 (not necessarily an integral number!) showed that boundaries of the clusters of two types are dual [43]. The first is the geometric cluster, which consists of neighboring spins of identical color. The second is the Fortuin–Kasteleyn cluster, which contains a smaller number of spins and is sparser than the geometric cluster, since some nearest-neighbor spins are unaligned (uncorrelated) owing to interaction with the heat bath. Identification of these clusters on the medial lattice is unambiguous and uses a well-defined algorithm [43]. Many scenarios for defining the boundaries of clusters on a lattice have been discussed in the literature on random fractal clusters. They are essentially reducible to the above-described boundaries of two clusters.

3.7 Critical amplitudes

I will briefly mention the work on the computation of universal ratios between critical amplitudes, which has been progressing very vigorously in recent years. This field requires a special review. A brief overview of the current status of numerical studies can be found in Ref. [44].

3.8 Problem of diffusion-limited aggregation

The problem of structure growth through diffusion is well defined in the two-dimensional case. It can be formulated as a random walk in an infinite plane with a particle sticking to the growing seed on contact. The probability of the particle escaping to infinity is zero, i.e., during the random walk (which can be arbitrarily long) the particle will eventually come in contact with the cluster boundary, so the cluster grows by one particle. This formulation allows the construction of an algorithm which ensures any required accuracy of obeying boundary conditions. This is important, because such a walk is described by the solution of the two-dimensional Laplace equation with two boundary conditions: on the boundary of the growing cluster, and at infinity; we know that this solution may lead to explosive instability. An algorithm was suggested in Ref. [45] which accurately implements such boundary conditions for simulating random diffusion-limited aggregation (DLA) [46].

To compute the fractal dimension of such clusters, we need to analyze a great number of large-sized clusters. Such simulation can be successfully realized in a computing cluster, specially designed for the type of problems in which every node possesses a large amount of RAM (4 gigabytes per thread), which makes it possible to commit to memory the entire computational structure of a cluster comprising up to a billion particles. For each value of the parameter, we generated a thousand clusters containing a hundred million particles each. An analysis of these clusters using a specially developed probe particle technique [47] made it possible to build a morphological histogram, shown in Fig. 3 and providing a qualitative description of the first-order phase transition between symmetrically arranged clusters and random clusters in the plane of two parameters — the coefficient of adhesion, and the symmetry of the external crystal field (such as that of the crystalline substrate on which diffusion unfolds) [48].

An investigation of the probability of growth of the emerging clusters allowed us to disprove in the DLA framework the hypothesis of multiscaling of random growth

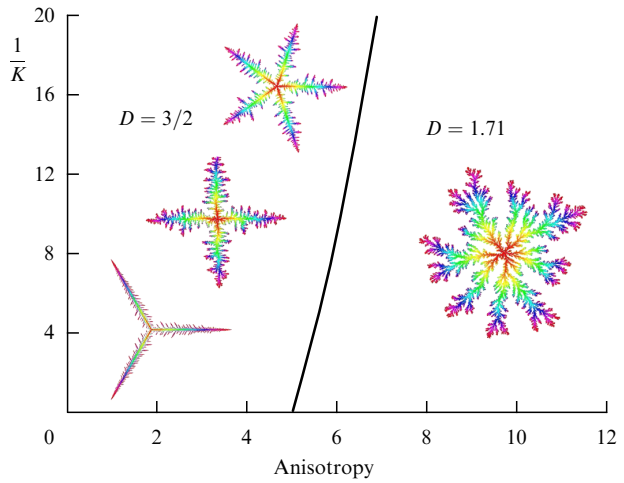

Figure 3. Morphological diagram of growth patterns of random clusters through diffusion. The horizontal axis specifies the symmetry of the external crystal field. The vertical axis is the inverse coefficient of particle adhesion. The solid line fits the line of first-order phase transition. D denotes the value of the fractal dimension of clusters in the thermodynamic limit.

clusters and to identify a scale-invariant form of the probability of a particle attachment to a cluster [49].

4. Conclusion

The examples given above conclusively demonstrate that computational physics can be successfully applied to testing theoretical hypotheses and predictions in various fields of physics.

The application of specialized computing machines has proved to be very successful in a number of cases. It should be noted that an elevated level of specialization, demanding a relatively high investment of intellectual effort, leads to the creation of machines whose usefulness for research is limited in time. However, even though their effective employment does not stretch beyond five or six years, during which they outperform all other computational systems, they may help in obtaining important scientific results much earlier than by using other approaches.

In 1996, the International Union of Pure and Applied Physics (IUPAP) created Commission C20 on Computational Physics [50]. Its task is to conduct annual conferences on computational physics. Conferences are held alternately in three geographic sectors — North and South America, Asia and Oceania, and Europe and Africa. Next year, in 2013, the conference will be conducted by the Russian Academy of Sciences in Moscow, which will give Russian scientists a chance to present to the international community their achievements in the field of computational physics.

The author is grateful to the RF Ministry of Education and Science for its support of this project (government contract No. 07.514.11.4032).

References

1. Fermi E, Pasta J, Ulam S "Studies of nonlinear problem", Los Alamos Sci. Lab. Rep. LA-1940 (Los Alamos: Los Alamos Sci. Lab., 1955)
2. Harlow F H, Metropolis N "Computing & computers: Weapons simulation leads to the computer era" *Los Alamos Science* (Winter/Spring) 132 (1983); http://library.lanl.gov/cgi-bin/getfile?07-15.pdf
3. Zabusky N J, Kruskal M D *Phys. Rev. Lett.* **15** 240 (1965)
4. Gardner C S et al. *Phys. Rev. Lett.* **19** 1095 (1967)
5. Zakharov V E et al. *Teoriya Solitonov: Metod Obratnoi Zadachi Rasseyaniya* (Theory of Solitons: Inverse Scattering Method) (Moscow: Nauka, 1980)
6. Metropolis N et al. *J. Chem. Phys.* **21** 1087 (1953)
7. Manakov S V, Shchur L N *Pis'ma Zh. Eksp. Teor. Fiz.* **37** 45 (1983) [*JETP Lett.* **37** 54 (1983)]
8. Poincaré H *Les Méthodes Nouvelles de la Mécanique Céleste* (New Methods of Celestial Mechanics) (Paris: Gauthier-Villars et fils, 1899) [Translated into English (Washington: NASA, 1960); Translated into Russian (Moscow: Nauka, 1971)]
9. Nikolaevskii E S, Shchur L N *Pis'ma Zh. Eksp. Teor. Fiz.* **36** 176 (1982) [*JETP Lett.* **36** 218 (1982)]
10. Belinskii V A, Lifshitz E M, Khalatnikov I M *Usp. Fiz. Nauk* **102** 463 (1970) [*Sov. Phys. Usp.* **13** 745 (1971)]
11. Lifshitz E M, Lifshits I M, Khalatnikov I M *Zh. Eksp. Teor. Fiz.* **59** 322 (1970) [*Sov. Phys. JETP* **32** 173 (1971)]
12. Lifshitz E M et al. *Pis'ma Zh. Eksp. Teor. Fiz.* **38** 79 (1983) [*JETP Lett.* **38** 91 (1983)]
13. Shchur L N *Comput. Phys. Commun.* **121 – 122** 83 (1999)
14. Barash L, Shchur L N *Phys. Rev. E* **73** 036701 (2006)
15. Barash L Yu, Shchur L N *Comput. Phys. Commun.* **182** 1518 (2011)
16. Reidler I et al. *Phys. Rev. Lett.* **103** 024102 (2009)
17. Onsager L *Phys. Rev.* **65** 117 (1944)
18. Dotsenko Vik S, Dotsenko V S *Adv. Phys.* **32** 129 (1983)
19. Talapov A L, Andreichenko V B, Dotsenko Vl S, Shchur L N *Pis'ma Zh. Eksp. Teor. Fiz.* **51** 161 (1990) [*JETP Lett.* **51** 182 (1990)]
20. Kirkpatrick S, Stoll E P *J. Comput. Phys.* **40** 517 (1981)
21. Talapov A L, Shchur L N, Andreichenko V B, Dotsenko Vl S *Mod. Phys. Lett. B* **6** 1111 (1992)
22. Talapov A L, Shchur L N *J. Phys. Condens. Matter* **6** 8295 (1994)
23. Talapov A L, Shchur L N *Europhys. Lett.* **27** 193 (1994)
24. Plechko V N *Phys. Lett. A* **239** 289 (1998)
25. Andreichenko V B et al. *Nucl. Phys. B* **344** 531 (1990)
26. Shchur L N, Vasilyev O A *Phys. Rev. E* **65** 016107 (2002)
27. Le Guillou J C, Zinn-Justin J *J. Physique* **48** 19 (1987)
28. Campostrini M et al. *Phys. Rev. E* **65** 066127 (2002)
29. Landau D P *Physica A* **205** 41 (1994)
30. Talapov A L, Blöte H W J, Shchur L N *Pis'ma Zh. Eksp. Teor. Fiz.* **62** 157 (1995) [*JETP Lett.* **62** 174 (1995)]
31. Shchur L N, Blöte H W J *Phys. Rev. E* **55** R4905 (1997)
32. Blöte H W J, Shchur L N, Talapov A L *Int. J. Mod. Phys. C* **10** 1137 (1999)
33. Aizenman M, in *Statphys 19: Proc. of the 19th IUPAP Intern. Conf. on Statistical Physics, Xiamen, China, July 31 – August 4, 1995* (Ed. H Bai-Lin) (Singapore: World Scientific, 1996)
34. Shchur L N, Kosyakov S S *Int. J. Mod. Phys. C* **8** 473 (1997)
35. Cardy J *J. Phys. A Math. Gen.* **31** L105 (1998)
36. Shchur L N, Rostunov T *Pis'ma Zh. Eksp. Teor. Fiz.* **76** 553 (2002) [*JETP Lett.* **76** 475 (2002)]
37. Mandelbrot B B *Physica A* **191** 95 (1992)
38. Belavin A A, Polyakov A M, Zamolodchikov A B *Nucl. Phys. B* **241** 333 (1984)
39. Dotsenko Vl S, Fateev V A *Nucl. Phys. B* **240** 312 (1984)
40. Schramm O *Isr. J. Math.* **118** 221 (2000)
41. Smirnov S, in *Proc. of the Intern. Congress of Mathematicians (ICM), Madrid, Spain, August 22 – 30, 2006* Vol. II (Helsinki: The European Mathematical Soc., 2006) p. 1421; http://www.icm2006.org/proceedings/Vol_II/contents/ICM_Vol_2_68.pdf
42. Duplantier B *Phys. Rev. Lett.* **84** 1363 (2000)
43. Zatelepin A, Shchur L, arXiv:1008.3573
44. Shchur L N, Janke W *Nucl. Phys. B* **840** 491 (2010)
45. Menshutin A Yu, Shchur L N *Phys. Rev. E* **73** 011407 (2006)
46. Witten T A (Jr.), Sander L M *Phys. Rev. Lett.* **47** 1400 (1981)
47. Menshutin A Yu, Shchur L N, Vinokur V M *Phys. Rev. E* **75** 010401(R) (2007)
48. Menshutin A Yu, Shchur L N *Comput. Phys. Commun.* **182** 1819 (2011)
49. Menshutin A *Phys. Rev. Lett.* **108** 015501 (2012)
50. Commission on Computational Phys. (C20), http://www.iupap.org/commissions/c20/members/index.html